J. Fluid Mech. (2023), *vol*. 959, A8, doi:10.1017/jfm.2023.125

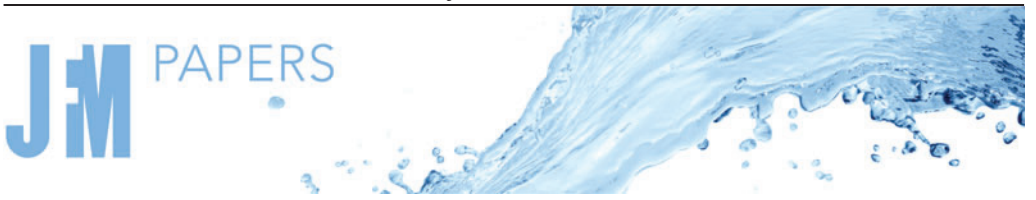

Heat-transfer scaling at moderate Prandtl numbers in the fully rough regime

Kevin Zhong[1],†, **Nicholas Hutchins**[1] **and Daniel Chung**[1]

[1]Department of Mechanical Engineering, University of Melbourne, Victoria 3010, Australia

(Received 24 January 2022; revised 28 October 2022; accepted 25 January 2023)

In the fully rough regime, proposed models predict a scaling for a roughness heat-transfer coefficient, e.g. the roughness Stanton number $St_k \sim (k^+)^{-p} Pr^{-m}$ where the exponent values p and m are model dependent, giving diverse predictions. Here, k^+ is the roughness Reynolds number and Pr is the Prandtl number. To clarify this ambiguity, we conduct direct numerical simulations of forced convection over a three-dimensional sinusoidal surface spanning $k^+ = 5.5$–111 for Prandtl numbers $Pr = 0.5$, 1.0 and 2.0. These unprecedented parameter ranges are reached by employing minimal channels, which resolve the roughness sublayer at an affordable cost. We focus on the fully rough phenomenologies, which fall into two groups: $p = 1/2$ (Owen & Thomson, *J. Fluid Mech.*, vol. 15, issue 3, 1963, pp. 321–334; Yaglom & Kader, *J. Fluid Mech.*, vol. 62, issue 3, 1974, pp. 601–623) and $p = 1/4$ (Brutsaert, *Water Resour. Res.*, vol. 11, issue 4, 1975*b*, pp. 543–550). Although we find the mean heat transfer favours the $p = 1/4$ scaling, the Prandtl–Blasius boundary-layer ideas associated with the Reynolds–Chilton–Colburn analogy that underpin the $p = 1/2$ can remain an apt description of the flow locally in regions exposed to high shear. Sheltered regions, meanwhile, violate this behaviour and are instead dominated by reversed flow, where no clear correlation between heat and momentum transfer is evident. The overall picture of fully rough heat transfer is then not encapsulated by one singular mechanism or phenomenology, but rather an ensemble of different behaviours locally. The implications of the approach to a Reynolds-analogy-like behaviour locally on bulk measures of the Nusselt and Stanton numbers are also examined, with evidence pointing to the onset of a regime transition at even-higher Reynolds numbers.

Key words: turbulent convection, turbulence simulation, turbulent boundary layers

† Email address for correspondence: kevin.zhong@student.unimelb.edu.au

1. Introduction

The transport of scalars such as temperature (heat), contaminants and CO_2 are a key feature of many engineering and natural flows (Kays & Crawford 1993; Wyngaard 2010). It is often the case that these flows are both turbulent and involve a surface roughness (Chung *et al.* 2021), which further complicates the prediction of these flows. Here, we consider the advection of passive scalars (forced convection) for incompressible flows, defined by their relatively low concentrations with negligible buoyancy effects (Warhaft 2000). Forced convection regimes are representative of many industrial flows where energy is supplied to the system predominantly through shear such as pumps (Kays & Crawford 1993), and is also applicable to flow in the atmospheric surface layer, typically $O(100)$ m from the Earth's surface under near-neutral conditions (Wyngaard 2010). The assumptions of incompressible forced convection are violated typically in strongly heated flows where significant density variations can cause buoyancy forces to become active (Warhaft 2000) and in atmospheric flows at heights approaching the Obhukov height, L_O, such that $|z/L_O| \gtrsim 0.01$ (Wyngaard 2010). Such flows and those involving compressibility (high Mach number) lie beyond the scope of the present work. In a forced convection regime, the physical law governing the transport of mass and heat are identical, only differing by the value of the Prandtl number (or Schmidt number, Sc, for mass transfer), $Pr \equiv \nu/\alpha$, where ν is the kinematic viscosity and α its thermal (or mass) diffusivity. This equivalence permits us to refer to both heat and mass transfer at the same time and we will refer to only the former henceforth.

The presence of roughness elements will give rise to a drag penalty, $\Delta U^+(k^+)$, which manifests as a downward shift in the logarithmic smooth-wall mean velocity profile (Clauser 1954; Hama 1954):

$$U^+ \equiv \frac{U}{U_\tau} = \frac{1}{\kappa}\log[(z-d)^+] + A - \Delta U^+(k^+), \tag{1.1a}$$

$$= \frac{1}{\kappa}\log[(z-d)/z_0], \tag{1.1b}$$

$$= \frac{1}{\kappa}\log[(z-d)/k_s] + A_{FR}, \tag{1.1c}$$

where the mean streamwise velocity, U, is normalised by the friction velocity, $U_\tau \equiv \sqrt{\langle\tau_w\rangle/\rho}$, associated with the integrated wall shear stress per unit plan area, $\langle\tau_w\rangle$, and fluid density, ρ, with the von Kármán constant, $\kappa \approx 0.4$, and the smooth-wall log intercept, $A \approx 5.0$. The wall shear stress is defined to include contributions from both pressure drag, τ_p, and viscous drag, τ_ν, such that $\langle\tau_w\rangle \equiv \langle\tau_p\rangle + \langle\tau_\nu\rangle$. We use $+$ superscripts to denote quantities normalised by U_τ and ν. The wall-normal distance (z-direction) is measured from the roughness virtual origin, $z-d$, where d represents a wall-normal shift relative to a reference z-location (Perry & Joubert 1963; Raupach, Antonia & Rajagopalan 1991; Luchini 1996; Nikora *et al.* 2002) to be defined more formally in § 3.2. The quantity ΔU^+ is commonly referred to as the roughness function (Clauser 1954; Hama 1954) and depends on the roughness Reynolds number, $k^+ \equiv kU_\tau/\nu$, where k is a representative size for the rough surface, e.g. the peak-to-trough roughness height. The alternative formulations provided in (1.1*b*) and (1.1*c*) use the roughness length for momentum, z_0, and equivalent sand-grain roughness, k_s, with intercept, $A_{FR} \approx 8.5$ (Nikuradse 1933; Schlichting 1936). The former is commonly used in meteorology (Raupach *et al.* 1991; Brutsaert 1982; Wyngaard 2010), whereas the latter is typical for engineering applications and is exclusive to the fully rough regime (Jiménez 2004; Chung *et al.* 2021). By combining (1.1*a*)–(1.1*c*),

we can relate ΔU^+, k_s^+ and z_0^+. Namely, $k_s^+ = \exp[\kappa(\Delta U^+ - A + A_{FR})]$, $k_s^+/z_0^+ = \exp(\kappa A_{FR}) \approx 30$, such that knowledge of either z_0^+ or k_s^+ for a flow is equivalent to knowing ΔU^+. Generally, ΔU^+ will depend on as many length scales that are required to fully describe the rough surface in question (Raupach *et al.* 1991; Jiménez 2004; Flack & Schultz 2010; Chung *et al.* 2021), but for geometrically similar rough surfaces, as is the case in the present work, this dependency is reduced to a single length scale, k.

In addition to altering momentum transfer, rough surfaces also augment heat transfer at solid interfaces (Bons *et al.* 2001). By analogy to the momentum transfer problem, this can be represented as an offset relative to a logarithmic smooth-wall temperature profile (Dipprey & Sabersky 1963; Yaglom & Kader 1974; Yaglom 1979; Kader 1981; Brutsaert 1982; Kays & Crawford 1993):

$$\Theta^+ \equiv \frac{\Theta}{\Theta_\tau} = \frac{1}{\kappa_\theta}\log[(z-d)^+] + A_\theta(Pr) - \Delta\Theta^+(k^+, Pr), \tag{1.2a}$$

$$= \frac{1}{\kappa_\theta}\log[(z-d)/z_0] + St_k^{-1}(k^+, Pr), \tag{1.2b}$$

$$= \frac{1}{\kappa_\theta}\log[(z-d)/k_s] + g(k^+, Pr), \tag{1.2c}$$

$$= \frac{1}{\kappa_\theta}\log[(z-d)/z_i] + \Theta_i^+(k^+, Pr), \tag{1.2d}$$

with $\kappa_\theta \approx 0.46$ (Pirozzoli, Bernardini & Orlandi 2016) and Θ representing the mean temperature relative to the wall temperature. The smooth-wall log intercept, $A_\theta(Pr)$, depends on the Prandtl number, Pr, and roughness introduces a heat-transfer augmentation, $\Delta\Theta^+(k^+, Pr)$, relative to this intercept. The quantity $\Theta_\tau \equiv \langle q_w\rangle/(\rho c_p U_\tau)$ is the friction temperature, with $\langle q_w\rangle$ representing the wall heat flux (defined in (2.2*a*)) and c_p the specific heat at constant pressure. Here, we measure from the same virtual origin location, $z-d$, as that of the velocity in (1.1), assuming the virtual-origin shift, d, to be identical for both velocity and temperature. In (1.2*b*)–(1.2*d*), we provide alternative formulations that appear in the literature: formulations for the inverse roughness Stanton number, St_k^{-1} (also written as B^{-1} in the atmospheric sciences), using z_0 coordinates (Jayatilleke 1966; Garratt & Hicks 1973; Kays & Crawford 1993; Kanda *et al.* 2007; Anderson 2013), the g-function (Dipprey & Sabersky 1963; Owen & Thomson 1963; Webb, Eckert & Goldstein 1971; Yaglom & Kader 1974) using k_s and the formulation based on an interfacial height, z_i, defined as the height above which the temperature profile is logarithmic with its accompanying interfacial temperature at this height, Θ_i (elaborated further in § 2) (Owen & Thomson 1963; Yaglom & Kader 1974; Brutsaert 1975*a*,*b*). The various log-intercepts are related by combining (1.2*b*)–(1.2*d*), e.g. $St_k^{-1} = (1/\kappa_\theta)\log(z_0/k_s) + g \approx g - 7.4$, $St_k^{-1} = (1/\kappa_\theta)\log(z_0/z_i) + \Theta_i^+$. Unlike with z_0 and k_s, which can be linked through $k_s/z_0 \approx 30$, z_i does not have any fixed relation to z_0 or k_s (Brutsaert 1975*b*, 1982). Some authors in their theories however, (e.g. Owen & Thomson 1963; Yaglom & Kader 1974) adopted (1.2*d*) as a starting point, and then set $z_i = k_s$ so $\Theta_i^+ = g$.

Progress in our understanding of momentum transfer (drag) and heat transfer has been largely disparate. The behaviour of ΔU^+ is well documented in the literature and has been extensively reviewed (e.g. Raupach *et al.* 1991; Jiménez 2004; Flack & Schultz 2010; Chung *et al.* 2021). Since the seminal works of Nikuradse (1933); Schlichting (1936), it is established that for rough surfaces in the fully rough regime, pressure drag acts

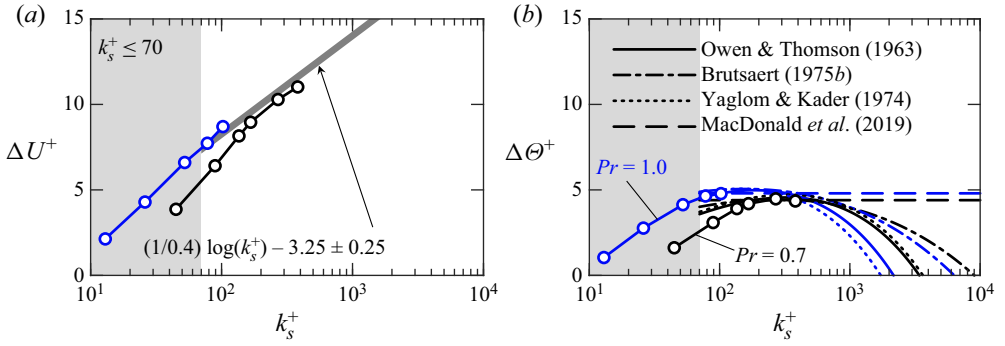

Figure 1. (*a*) Typical behaviour of ΔU^+ in the fully rough regime showing direct numerical simulation (DNS) data for a sinusoidal surface (black circles) (MacDonald, Hutchins & Chung 2019) and irregular roughness (blue circles) (Peeters & Sandham 2019). The $k_s^+ \leq 70$ range is demarcated with the grey box and corresponds to the conventional threshold below the fully rough regime (Flack & Schultz 2010). (*b*) Disparate predictions of fully rough $\Delta\Theta^+$ models. The model constants are fitted to the DNS data for $Pr = 0.7$ (black) from MacDonald *et al.* (2019) and $Pr = 1.0$ (blue) from Peeters & Sandham (2019). For $Pr = \{0.7, 1.0\}$, the model constants are $C'_R = \{0.3, 0.3\}$, $D'_R = \{7.2, 8.4\}$ for $g = C'_R(k_s^+)^{1/2}Pr^{2/3} + D'_R$ in Owen & Thomson (1963), $C_R = \{2.5, 2.4\}$, $D_R = \{2.7, 3.7\}$ for $\Theta_i^+ = C_R(k_s^+)^{1/4}Pr^{1/2} + D_R$ in Brutsaert (1975*b*) assuming $z_i = k_s$, and $b'_1 = \{0.6, 0.5\}$, $b'_2 = \{0.4, 0.3\}$, $b'_3 = \{7.1, 7.8\}$ for $g = b'_1(k_s^+)^{1/2}(Pr^{2/3} - b'_2) + b'_3$ in Yaglom & Kader (1974), and $\Delta\Theta^+ = \{4.4, 4.8\}$ in MacDonald *et al.* (2019).

as the dominant contribution to skin friction and their mean-flow behaviour follows a log-linear relation, $U^+ = (1/\kappa)\log[(z-d)/k] + C$, where C is a constant that depends on the roughness geometry independent of viscous effects (Jiménez 2004). The universality of this behaviour is exploited by passing from k to k_s via $C \equiv (1/\kappa)\log(k/k_s) + A_{FR}$, which allows for ΔU^+ measurements of roughness from different types to collapse onto a single, universal asymptote using k_s as the reference scale (figure 1*a*).

Our understanding of $\Delta\Theta^+$, by contrast, has not seen the same degree of progress. Whereas pressure drag makes the dominant contribution to drag in the fully rough regime (Jiménez 2004; Flack & Schultz 2010), an analogue for pressure drag does not exist in heat transfer (Dipprey & Sabersky 1963; Owen & Thomson 1963). Heat transfer at the solid surface occurs solely through molecular conduction and this is reflected in not only the dependence on k^+ but also the dependence on Pr, which includes the thermal diffusivity, α. The underlying asymptotic form of $\Delta\Theta^+$ in the fully rough regime remains ambiguous with disagreement amongst current models (figure 1*b*). Empirical models for rough-wall heat transfer have typically been restricted to fit data of single roughness types and their universality cannot be guaranteed (e.g. Dipprey & Sabersky 1963; Jayatilleke 1966; Webb *et al.* 1971; Dawson & Trass 1972; Garratt & Hicks 1973; Kays & Crawford 1993). Phenomenological models, some of which are shown in figure 1(*b*), have also emerged. Unlike the empirical formulations, the physical assumptions leading to these model predictions provide a basis for scrutiny and will be the focus of this paper.

The phenomenological model of Yaglom & Kader (1974) takes the form $g = b'_1(k_s^+)^{1/2}(Pr^{2/3} - b'_2) + b'_3$ in (1.2*c*) and is obtained through scaling arguments, where b'_1, b'_2 and b'_3 are fitting constants. Later, the same authors amend this expression by introducing a fitting parameter, γ, to replace the original 1/2 exponent, giving $g = b'_1(k_s^+)^{\gamma}(Pr^{2/3} - b'_2) + b'_3$ (Kader & Yaglom 1977). They allowed $\gamma = 1/4$ for better agreement with two-dimensional (2-D)-roughness, arguing that γ could take the value

of either 1/2 or 1/4 depending on whether three-dimensional (3-D)- or 2-D-roughness is being considered, but later, Yaglom (1979) concedes the crude nature of categorising all roughness types into these two subsets, noting that the universality of these expressions is suspect. Recently, the direct numerical simulation (DNS) study of MacDonald *et al.* (2019) observed a thin conductive sublayer that conforms to the roughness topography in the fully rough regime. This led them to postulate that the temperature field behaves as though the rough wall is effectively smooth on the increased surface area so that $\Delta\Theta^+$ attains a constant value. This was one of the hypotheses proposed by Sverdrup (1951), but limited data availability prevented concrete conclusions on the certainty of this form. Interfacial temperature formulations (1.2*d*), discussed in § 2, take the form $\Theta_i^+ = C_R(k^+)^p Pr^m + D_R$, where C_R and D_R are constants dependent on roughness geometry, and p and m are exponents determined by phenomenological arguments (Owen & Thomson 1963; Brutsaert 1975*b*). The appropriate values to take for p and m is an ongoing topic of debate (Li *et al.* 2017, 2020) and we will dedicate § 2 towards elaborating on the diverse perspectives. To demonstrate this, we show in figure 1(*b*) the $Pr = O(1)$ formulation of Owen & Thomson (1963) who propose $p = 1/2$, $m = 2/3$ and of Brutsaert (1975*b*) who proposes $p = 1/4$, $m = 1/2$. Empirical expressions that have taken $\Theta_i^+ = g$ have also seen diverse values proposed for the exponents, with $p = 0.2$–0.5, $m = 0.44$–0.8 (Dipprey & Sabersky 1963; Sheriff & Gumley 1966; Webb *et al.* 1971; Dawson & Trass 1972). Inspection of $\Delta\Theta^+$ trends in figure 1(*b*) with respect to model predictions alone is not sufficient in telling us what the appropriate scaling exponents should be, as the model constants can be tuned to fit a particular dataset.

Rather than merely compare model predictions, a more robust approach is to test the underlying physical assumptions which underpin these models. However, the hypothesised mechanisms involved have remained difficult to interrogate due to a lack of high-fidelity data in the fully rough regime, alongside insufficient Prandtl number variations. Although recent DNS studies (e.g. Leonardi *et al.* 2015; Orlandi, Sassun & Leonardi 2016; Forooghi, Stripf & Frohnapfel 2018*a*; Forooghi *et al.* 2018*b*; MacDonald *et al.* 2019; Peeters & Sandham 2019; Hantsis & Piomelli 2020) have helped to further advance our understanding of rough-wall heat transfer, a systematic sweep of the (k^+, Pr) parameter space that is necessary to scrutinise these hypothesised mechanisms has yet to emerge. Not only is the 2-D (k^+, Pr) parameter space expensive to sample, the unfavourable $O(Re_\tau^{9/4})$ computational cost of resolving the momentum field in a smooth-wall DNS flow (Pope 2000, § 9.1.2) is further increased to $O(Re_\tau^{9/4} Pr^{3/2})$ for $Pr \gtrsim 1$ simulations (Yano & Kasagi 1999), where Re_τ is the friction Reynolds number.

Our present work will circumvent these stringent computational costs by employing minimal channel simulations, which only capture the near-wall flow by constraining the channel domain size (Chung *et al.* 2015; MacDonald *et al.* 2017, 2019). The assumption which underpins this approach lies in Townsend's outer-layer similarity hypothesis (Townsend 1976), which states that roughness serves to predominantly alter only the flow confined to the near-wall region. The outer layer remains insensitive to roughness except for how it sets the friction velocity U_τ, and outer-layer details are unimportant in studying the effects of roughness. More recently, DNS studies have emerged which corroborate that outer-layer similarity can be generalised to heat transfer (Doosttalab *et al.* 2016; MacDonald *et al.* 2019; Hantsis & Piomelli 2020), so that the minimal channel approach can provide an efficient method to sweep the (k^+, Pr) parameter space. With a comprehensive DNS dataset to work with, we will scrutinise the proposed phenomenologies that describe rough-wall heat transfer, so that the underlying mechanisms can be resolved.

The paper is organised as follows. We summarise the key competing phenomenologies in § 2. Our DNS data are detailed in § 3, with § 4 dedicated to addressing our primary research questions concerning the phenomenology of heat transfer. As we shall see, although the phenomenological model of Brutsaert (1975*b*) will be favoured when we consider measures of the total heat transfer, certain phenomenological ideas in the contrary theories of Owen & Thomson (1963) and Yaglom & Kader (1974) can remain robust when examining the flow locally. We investigate the implications this has on full-scale heat transfer prediction in § 5, through bulk measures of the Nusselt and Stanton numbers. We provide conclusions in § 6.

2. Fully rough models for rough-wall heat-transfer

2.1. *Mean scaling laws in terms of local quantities*

The influence of rough walls on heat transfer is encapsulated in any of the logarithmic intercepts in (1.2*a*)–(1.2*d*). We will focus on the (1.2*d*) formulation, which makes use of the interfacial height, z_i, defined to be the height above which the temperature profile is logarithmic and homogeneous (Brutsaert 1975*b*). The interfacial temperature at this height is described through a power law formulation $\Theta^+(z-d=z_i)\equiv\Theta_i^+\sim(k^+)^pPr^m$. The correct values to take for p and m have been a topic of contention (Li *et al.* 2017, 2020) and one of our main contributions in the present work will be to provide evidence towards resolution. A sketch of the physical picture using this (z_i,Θ_i) framework is provided in figure 2(*a*). Provided Θ_i^+ and z_i^+ are known as a function of k^+ and Pr, the procedure thereafter falls to matching at z_i^+ with the logarithmic profile using the value Θ_i^+, which is equivalent to prescribing the logarithmic intercept. The region below z_i is assumed to be well mixed, having uniform temperature Θ_i, but closer to the wall, there will exist the conductive sublayer of thickness δ_θ submerged below z_i. In the case of $Pr\ll 1$ such as for liquid metals, the effects of molecular conduction may extend beyond the expected extent of the logarithmic temperature profile, invalidating the concept of z_i (Alcántara-Ávila, Hoyas & Pérez-Quiles 2018; Abe & Antonia 2019). In such instances, the framework in figure 2(*a*) will no longer hold so the case of $Pr\ll 1$ will not be treated.

To probe local mechanisms pertinent to the phenomenologies, it is useful to adopt a local conductive sublayer thickness, δ_θ:

$$\delta_\theta(x,y)=\frac{\theta_{\delta_\theta}(x,y)}{\partial\theta/\partial n|_w}\approx\frac{\Theta_i}{\partial\theta/\partial n|_w},\tag{2.1}$$

where $\partial\theta/\partial n|_w$ is the local wall-normal temperature gradient at the rough wall, θ_{δ_θ} is the local temperature at the edge of the conductive sublayer and x–y are streamwise-spanwise coordinates. Equation (2.1) takes δ_θ to be the intersection point between the tangent of the local temperature profile with θ_{δ_θ}. By consequence of assuming a well-mixed roughness sublayer, this temperature is then taken to be $\theta_{\delta_\theta}\approx\Theta_i$ (figure 2*b*). This δ_θ definition corresponds to the so-called tangent method common in the Rayleigh–Bénard literature, where Θ_i coincides with the temperature in the bulk region (Zhou *et al.* 2010; Scheel & Schumacher 2014). The viscous sublayer thickness δ_ν is the linear region dominated by viscous diffusion and in separated regions, is somewhat ill-defined. The viscous sublayer is meaningful primarily in attached regions, which tend to form only in the exposed, windward regions experiencing favourable pressure gradients, as envisioned in figure 2(*a*).

Assuming the region below z_i to be well mixed except through the conductive sublayer, δ_θ, in which the temperature varies linearly, the local heat transfer can be inferred through Fourier's conduction law: $q_w/(\rho c_p)=\alpha\Theta_i/\delta_\theta$ (Owen & Thomson 1963;

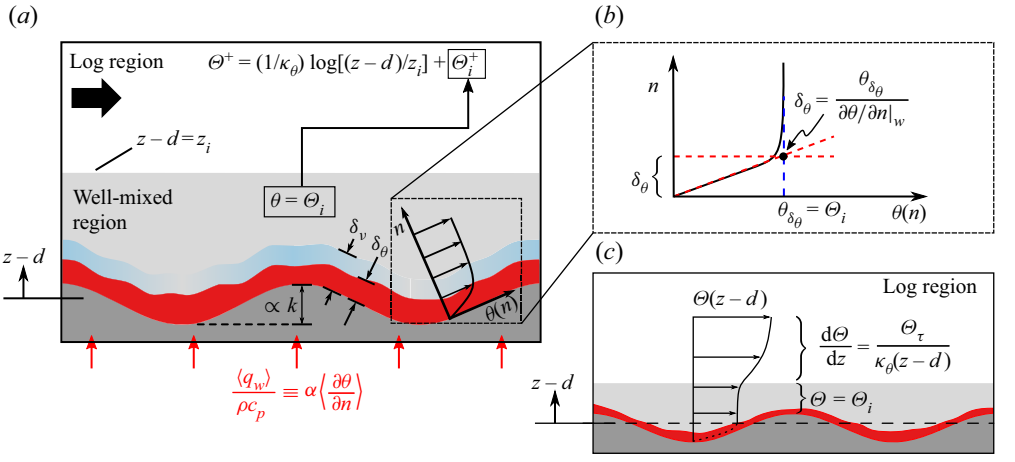

Figure 2. (*a*) Sketch of the problem set-up used in fully rough phenomenologies. The flow is partitioned into two regions by the height z_i, above which the temperature profile is logarithmic. The task falls to prescribing a phenomenology which describes the well-mixed region $z-d \le z_i$ (light grey) to obtain the temperature Θ_i, given the roughness size k and wall heat-flux $\langle q_w\rangle$. The sketch presents a configuration where $Pr > 1$, such that the conductive sublayer (red) is below z_i. (*b*) An example profile for the local wall-normal temperature profile, $\theta(n)$, showing how this problem can be reinterpreted in terms of the conductive sublayer thickness (2.1). A well-mixed roughness sublayer implies the temperature at the edge of the conductive sublayer, θ_{δ_θ}, is taken to be Θ_i. (*c*) A prototypical sketch of the mean temperature, Θ, measured from the virtual origin plane (dashed line) $z-d$. The origin coincides with the wall-origin perceived by the turbulent eddies in the logarithmic region (Nikora *et al.* 2002; Chung *et al.* 2021), which is assumed to be identical for both mean velocity and temperature (i.e. $d_\theta = d$).

Yaglom & Kader 1974; Brutsaert 1975*b*), the global effect of which can be obtained via integration as follows. By changing from the spatially homogeneous Θ_i to δ_θ, local variations arising due to roughness inhomogeneities can be examined:

$$\frac{\langle q_w\rangle}{\rho c_p} \equiv \frac{A_w}{A_t}\frac{1}{A_w}\int_{A_w} \alpha \left.\frac{\partial\theta}{\partial n}\right|_w \mathrm{d}A_w \tag{2.2a}$$

$$= \frac{A_w}{A_t}\alpha\Theta_i\frac{1}{A_w}\int_{A_w}\frac{1}{\delta_\theta}\mathrm{d}A_w \tag{2.2b}$$

$$\equiv \frac{A_w}{A_t}\alpha\Theta_i\left\langle\frac{1}{\delta_\theta}\right\rangle_w. \tag{2.2c}$$

Here, A_w is the wetted area, defined as the total rough-wall surface area in contact with the working fluid and A_t is the plan (or projected) area, with the ratio A_w/A_t staying a fixed constant for a given roughness geometry. The expression (2.2*a*) is the physical definition of the heat flux, whilst to obtain (2.2*b*), we have substituted (2.1) into (2.2*a*). We use $\langle\cdot\rangle_w \equiv (1/A_w)\int_{A_w}(\cdot)\,\mathrm{d}A_w$ to denote the average over the wetted area, as in (2.2*c*), and $\langle\cdot\rangle \equiv (1/A_t)\int_{A_w}(\cdot)\,\mathrm{d}A_w$ for the wetted area integral normalised on the plan area. In non-dimensional units, (2.2*c*) reads:

$$\Theta_i^+ = Pr(A_t/A_w)\langle 1/\delta_\theta^+\rangle_w^{-1}. \tag{2.3}$$

We see from (2.3) that knowledge of the scaling $\langle 1/\delta_\theta^+\rangle_w \sim (k^+)^{-p}Pr^{1-m}$ would be equivalent to knowledge of the scaling $\Theta_i^+ \sim (k^+)^p Pr^m$. In general, $\langle\delta_\theta^+\rangle_w \neq \langle 1/\delta_\theta^+\rangle_w^{-1}$,

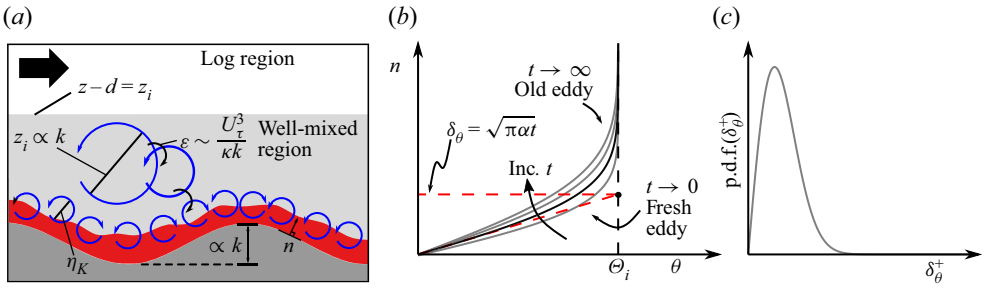

Figure 3. (*a*) Fully rough model of Brutsaert (1975*b*) which uses the Kolmogorov energy-cascade phenomenology. A scale separation forms between the roughness size k and the Kolmogorov-eddies which scour the surface area and have size η_K. The cascade is characterised by the rate of energy transfer ε. There exists an ensemble of these Kolmogorov eddies, each with their own contact time with the surface, t, and all of which initially carry temperature Θ_i from the well-mixed region, which we illustrate in (*b*). (*c*) Ensemble of Kolmogorov eddies represented by a probability density function (p.d.f.).

but many authors have neglected this distinction (Owen & Thomson 1963; Yaglom & Kader 1974). The approximation $\langle\delta_\theta\rangle_w \approx \langle 1/\delta_\theta\rangle_w^{-1}$ can be formally deduced by writing δ_θ in terms of a mean and fluctuation: $\delta_\theta \equiv \langle\delta_\theta\rangle_w + \delta_\theta''$ and letting $\epsilon \equiv \delta_\theta''/\langle\delta_\theta\rangle_w$, we perform a Taylor series expansion at $\epsilon = 0$ to obtain $\langle 1/\delta_\theta\rangle_w^{-1} = \langle\langle\delta_\theta\rangle_w^{-1}(1+\epsilon)^{-1}\rangle_w^{-1} = \langle\delta_\theta\rangle_w\langle 1-\epsilon+\epsilon^2+\ldots\rangle_w^{-1} \approx \langle\delta_\theta\rangle_w(1-\langle\epsilon^2\rangle_w) \approx \langle\delta_\theta\rangle_w$ for $\langle\epsilon^2\rangle_w \ll 1$. Thus, provided δ_θ does not deviate significantly from $\langle\delta_\theta\rangle_w$, one may expect the $\langle\delta_\theta^+\rangle_w = \langle 1/\delta_\theta^+\rangle_w^{-1}$ approximation to hold. Although we have presented a framework adopting (z_i^+, Θ_i^+), the $\Theta_i^+ \sim (k^+)^p Pr^m$ scaling law may be recast using any of the reference heights and logarithmic intercepts in (1.2*b*) and (1.2*c*). Recasting to the inverse roughness Stanton number and roughness length (z_0^+, St_k^{-1}), for instance, is done by combining (1.2*b*) and (1.2*d*) to obtain $St_k^{-1} = (1/\kappa_\theta)\log(z_0/z_i) + \Theta_i^+$. Provided z_0/z_i attains a constant value in the fully rough regime, this will result in $St_k^{-1} \sim \Theta_i^+ \sim (k^+)^p Pr^m$.

2.2. *The* 1/4 *Kolmogorov–Brutsaert scaling*

The 1/4 power law scaling picture, sometimes known as surface renewal theory (e.g. Brutsaert 1982; Katul & Liu 2017; Li *et al.* 2017, 2020) related to penetration theory (Danckwerts 1951; Bird, Stewart & Lightfoot 2007), was proposed for rough walls by Brutsaert (1975*b*). For this model, Brutsaert prescribes the energy cascade phenomenology of Kolmogorov (1941) to describe the well-mixed region, $z - d \leq z_i$. In the fully rough regime, a $k \gg \nu/U_\tau$ scale separation will develop and, as illustrated in figure 3(*a*), Brutsaert proposes that this roughness cascade starts at the beginning of the logarithmic region, z_i, which is assumed to be proportional to k, $z_i \propto k$. The cascade is characterised by a constant rate of energy transfer given by the turbulent dissipation rate $\varepsilon \approx U_\tau^3/(\kappa z_i) \propto U_\tau^3/(\kappa k)$ down to an ensemble of the smallest Kolmogorov eddies, having size $\eta_K \equiv (\nu^3/\varepsilon)^{1/4}$. The roughness elements provide a windless, stagnant shelter for these Kolmogorov eddies, which initially carry temperature Θ_i from the well-mixed region (grey region in figure 3*a*) and straddle the conductive sublayer. During the contact time, t, the Kolmogorov eddies give rise to a surface renewal process, depositing their temperature onto the rough surface in this windless environment that is everywhere without any viscous sublayer (compare figure 2*a* and figure 3*a*). Thus, in the absence of advection, the temperature they carry, θ, is modelled through an unsteady diffusion problem in

the local wall-normal direction n: $\partial\theta/\partial t = \alpha(\partial^2\theta/\partial n^2)$ with boundary conditions $\theta(n = 0, t) = 0$, $\theta(n > 0, t = 0) = \Theta_i$, $\theta(n \to \infty, t) = \Theta_i$. The latter two conditions reflect the notion that the Kolmogorov eddies exist in a well-mixed region and with the asymptotically large scale separation in the fully rough regime $z_i \gg \eta_K$, z_i can be interchanged with the far-field condition at $n \to \infty$ as both are large relative to the Kolmogorov eddy size. This is Stokes' first problem which has the solution $\theta(n, t) = \Theta_i \mathrm{erf}[n/(4\alpha t)^{1/2}]$ (figure 3*b*). Recall that t here is not understood as time elapsed, but rather the individual contact times of these Kolmogorov eddies. As seen in figure 3(*b*), fresh eddies from the well-mixed region initially carry a uniform temperature of Θ_i, which is gradually deposited over the duration of the contact period of the surface. The conductive sublayer thickness using this model is given by $\delta_\theta = (\pi\alpha t)^{1/2}$, obtained by combining (2.1) and $\partial\theta/\partial n|_w = \Theta_i/(\pi\alpha t)^{1/2}$ from the error function solution. The ensemble of these eddies and their respective contact times is represented by prescribing a probability density function, p.d.f.(t), or p.d.f.(δ_θ) equivalently. Here, Brutsaert (1975*b*) follows the same prescription originally proposed by Danckwerts (1951), whereby the stochastic nature of these eddy-renewal times follows an exponential probability distribution, with a mean contact time commensurate to the Kolmogorov time scale $t_\eta \equiv (\nu/\varepsilon)^{1/2}$. The mean heat flux is then obtained by Brutsaert (1975*b*) through an integration over the ensemble of contact times as prescribed by the exponential p.d.f. along with the solution $\partial\theta/\partial n|_w = \Theta_i/(\pi\alpha t)^{1/2}$, or alternatively, recast here also in terms of $\delta_\theta = (\pi\alpha t)^{1/2}$ and its p.d.f.:

$$\frac{\langle q_w\rangle}{\rho c_p} = \frac{A_w}{A_t}\int_0^\infty \alpha \left.\frac{\partial\theta}{\partial n}\right|_w \underbrace{\frac{1}{t_\eta}\exp\left(-\frac{t}{t_\eta}\right)}_{\text{p.d.f.}(t)}\mathrm{d}t \tag{2.4a}$$

$$= \frac{A_w}{A_t}\int_0^\infty \frac{\alpha\Theta_i}{\delta_\theta}\underbrace{\left[\frac{2}{\pi}\frac{\delta_\theta}{\eta_B^2}\exp\left(-\frac{\delta_\theta^2}{\pi\eta_B^2}\right)\right]}_{\text{p.d.f.}(\delta_\theta)}\mathrm{d}\delta_\theta \tag{2.4b}$$

$$= \frac{A_w}{A_t}\alpha\Theta_i\frac{1}{\eta_B}, \tag{2.4c}$$

where $\eta_B \equiv (\alpha t_\eta)^{1/2}$ is the Batchelor scale. Comparing (2.4*c*) with (2.2*c*), we identify $\langle 1/\delta_\theta\rangle_w = 1/\eta_B$. Finally, to obtain η_B, we insert $\varepsilon \sim U_\tau^3/(\kappa k)$ (figure 3*a*) into $t_\eta \equiv (\nu/\varepsilon)^{1/2}$ and $\eta_B \equiv (\alpha t_\eta)^{1/2}$. Letting $\langle 1/\delta_\theta\rangle_w = 1/\eta_B$, we obtain the scaling law for the inverse of the conductive sublayer thickness:

$$\langle 1/\delta_\theta\rangle_w = \alpha^{-1/2}\nu^{-1/4}\varepsilon^{1/4} \sim \alpha^{-1/2}\nu^{-1/4}U_\tau^{3/4}k^{-1/4} \tag{2.5a}$$

$$\implies \langle 1/\delta_\theta^+\rangle_w \sim (k^+)^{-1/4}Pr^{1/2}. \tag{2.5b}$$

Adopting (2.3), this resulting scaling predicts

$$\Theta_i^+ \sim St_k^{-1} \sim (k^+)^{1/4}Pr^{1/2}. \tag{2.6}$$

A limitation of this surface renewal model is that it does not distinguish between particular roughness locations and the potential for different renewal dynamics at these locations. The subtleties of these considerations, however, are hidden in the context of the final scaling law obtained in (2.5*b*) as noted by Katul & Liu (2017), as it is ultimately the mean value of $1/\delta_\theta$ that will yield the final scaling law.

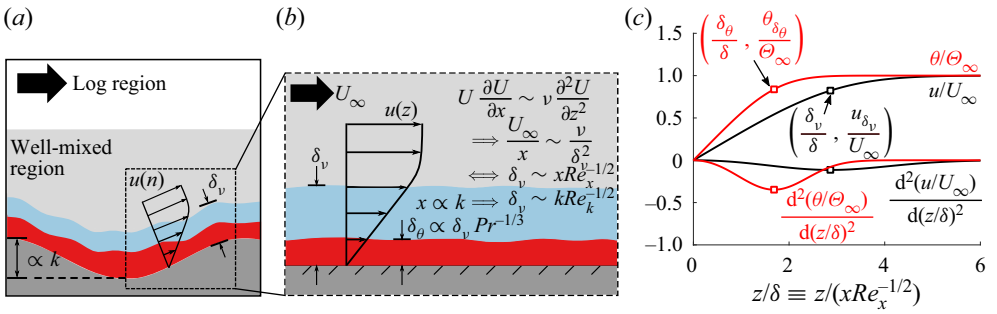

Figure 4. (*a*) A fully rough model sketch whereby Prandtl–Blasius-type laminar boundary layers, illustrated in (*b*), cover the entirety of the rough surface. The case is sketched for $Pr \gtrsim 1$ such that $\delta_\theta \propto \delta_\nu Pr^{m-1} = \delta_\nu Pr^{-1/3}$. (*c*) Example solutions from Prandtl–Blasius theory for velocity (black) and temperature (red) ($Pr = 5.0$). The linear viscous and conductive sublayer regions, δ_ν, δ_θ, respectively, are situated by the minima of second derivatives (square markers).

2.3. *The* 1/2 *Owen–Thomson scaling*

The 1/2 power law scaling for the fully rough regime draws on elements reminiscent of the Prandtl–Blasius laminar boundary layer theory (Schlichting & Gersten 2017) and is closely associated with the Reynolds–Chilton–Colburn analogy between heat or mass transfer and skin friction. The approach of authors proposing this method (e.g. Owen & Thomson 1963; Yaglom & Kader 1974) has been to generalise the scaling arguments of the Prandtl–Blasius solution to describe the local viscous sublayer, now assumed to cover the entirety of the rough surface (figure 4*a*,*b*) in contrast to surface renewal (figure 3*a*). In Prandtl–Blasius theory, the viscous sublayer thickness, δ_ν is (e.g. Landau & Lifshitz 1987):

$$\delta_\nu \sim xRe_x^{-1/2}, \quad Re_x \equiv xU_\infty/\nu, \tag{2.7a,b}$$

where x is the streamwise fetch, U_∞ is the free stream velocity and Re_x is the Reynolds number defined on these quantities. The result arises from laminar flow where streamwise advection balances wall-normal diffusion: $U(\partial U/\partial x) = \nu(\partial^2 U/\partial z^2)$, which implies $U_\infty^2/x \sim \nu U_\infty/\delta_\nu^2$ or (2.7*a*,*b*) equivalently after rearrangement. Here, a choice is made to link the viscous sublayer, δ_ν, and the usual laminar boundary-layer thickness, $\delta = xRe_x^{-1/2}$, in Prandtl–Blasius theory (Landau & Lifshitz 1987; Schlichting & Gersten 2017). The viscous sublayer, δ_ν, encapsulates the extent of the linear region where viscous stresses are most active and, as illustrated in figure 4(*c*), can be situated as the local minima of the second velocity derivative, $\mathrm{d}^2u/\mathrm{d}z^2$. For Prandtl–Blasius boundary-layers, one may adopt δ_ν and the velocity at this location, u_{δ_ν}, in replacement for the usual δ and U_∞ without loss of generality for scaling relations, as these quantities are related by a proportionality constant, $\delta_\nu/\delta \approx 2.9$, $u_{\delta_\nu}/U_\infty \approx 0.8$. Similar definitions for the conductive sublayer thickness, δ_θ, and its temperature, θ_{δ_θ}, may also be inferred from the second derivative minima (figure 4*c*, red). The advantage in adopting these viscous–conductive quantities as opposed to the free stream velocity U_∞ or boundary-layer thickness δ will be that these viscous–conductive quantities can be computed unambiguously in both a rough-wall flow and smooth-wall turbulent flow, providing a direct avenue to test the assumptions of a local Prandtl–Blasius or smooth-wall-like behaviour.

In the theories of Owen & Thomson (1963) and Yaglom & Kader (1974), it is proposed that the streamwise fetch x may be replaced by an arbitrary, but geometrical roughness

length scale: $x \propto k$, which physically implies that laminar boundary-layers will develop locally over distances proportional to k. This generalises the Prandtl–Blasius scaling of $\delta_\nu \sim xRe_x^{-1/2}$ to $\delta_\nu \sim kRe_k^{-1/2}$, where $Re_k \equiv ku_{\delta_\nu}/\nu$, a scaling which we may test explicitly in a rough-wall flow. The velocity scale $u_{\delta_\nu} \propto U_\tau$ is proposed, and reflects an intuition whereby U_τ represents the velocity scale directly above the viscous sublayer. Making these substitutions into (2.7*a*,*b*) enables a scaling with respect to k^+ to be obtained:

$$\delta_\nu \sim (\nu k/U_\tau)^{1/2}, \quad \delta_\nu^+ \sim (k^+)^{1/2} \tag{2.8a,b}$$

which was the result of Owen & Thomson (1963) and Yaglom & Kader (1974). However, the authors did not begin their arguments starting from the Prandtl–Blasius scaling of (2.7*a*,*b*) at the time, but rather by presuming that the flow within the viscous sublayer is characterised by $\mathrm{d}U/\mathrm{d}z \sim U_\tau/k$. As demonstrated by Yaglom & Kader (1974), this can be integrated to obtain $U \sim U_\tau z/k$. This velocity evaluated at δ_ν, $u_{\delta_\nu} = U_\tau \delta_\nu/k$, is used to define a Reynolds number scaled on the viscous sublayer quantities and is enforced to be of order unity: $Re_{\delta_\nu} \equiv u_{\delta_\nu}\delta_\nu/\nu = O(1)$, which implies $\delta_\nu \sim \nu/u_{\delta_\nu} = \nu k/(U_\tau \delta_\nu)$, an equivalent result to (2.8*a*,*b*). Recent studies concerning this scaling law (e.g. Li *et al.* 2017, 2020) interpret this as a case where the dynamics near the rough wall are driven primarily through the mean inverse time scale $\mathrm{d}U/\mathrm{d}z \sim U_\tau/k$, a so-called macro-eddy model. For laminar boundary-layers in general, $\delta_\theta \propto \delta_\nu Pr^{m-1}$, yielding the scaling for the conductive sublayer thickness $\delta_\theta^+ \sim (k^+)^{1/2}Pr^{m-1}$, as required in (2.3), to obtain for the heat transfer

$$\Theta_i^+ \sim St_k^{-1} \sim (k^+)^{1/2}Pr^m. \tag{2.9}$$

For the Prandtl number exponent m, Owen & Thomson (1963) proposed $m = 2/3$ for $Pr \gtrsim 1$ and $m = 3/4$ for $Pr \gg 1$, while Yaglom & Kader (1974) adopts a fixed $m = 2/3$ for $Pr \gtrsim 1$. In smooth-wall flows, the exponents $m = 1/2$ for $Pr \ll 1$ and $m = 2/3$ for $Pr \gg 1$ have been corroborated extensively by adopting Prandtl–Blasius-type arguments for laminar boundary-layers (Landau & Lifshitz 1987; Kays & Crawford 1993; Schlichting & Gersten 2017) and classical natural convection (Grossmann & Lohse 2000; Shishkina, Horn & Wagner 2013; Shishkina, Grossmann & Lohse 2016), and by assuming cubically increasing eddy diffusivities for the viscous–conductive sublayer region of turbulent flows (Kader 1981; Durbin & Pettersson-Reif 2011). The so-called Chilton–Colburn analogy for predicting heat transfer coincides with the case $m = 2/3$ (Kays & Crawford 1993; Bird *et al.* 2007). Some authors have also argued the case $m = 3/4$ for very large Pr (Lin 1959; Townsend 1976; Shaw & Hanratty 1977). MacDonald *et al.* (2019) observed a close analogy between local viscous and conductive fluxes, alongside an apparent saturation of the rough-wall heat transfer augmentation $\Delta\Theta^+$ to a constant value, which led the authors to postulate a local smooth-wall-like behaviour across the surface wetted area, implying that the same $\delta_\theta \propto \delta_\nu Pr^{m-1}$ relation for smooth walls may be found locally.

3. DNS dataset

3.1. *Simulation set-up*

We consider a channel flow with identical roughness topography at both top and bottom walls through a reflection at the channel centre-plane (figure 5*a*). The (x, y, z) directions are the streamwise, spanwise and wall-normal directions, respectively, with corresponding velocity components $\boldsymbol{u} = (u, v, w)$. The temperature, T, is considered a passive scalar and is decomposed as $T = \theta_w + \theta$, where θ_w is the wall temperature. We solve the governing

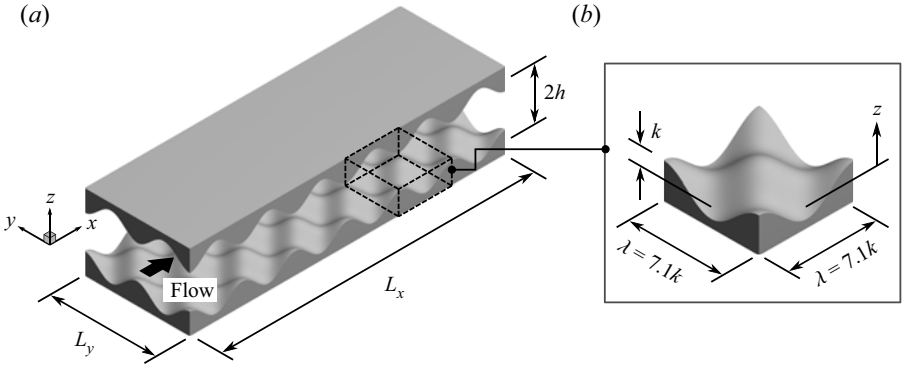

Figure 5. (*a*) Schematic of the computational domain. The channel half-height, h, is measured from the sinusoidal mid-plane to the channel centreline. (*b*) The present sinusoidal roughness, with amplitude, k, and wavelength, λ, as defined by (3.4). The wall-normal origin for z is taken to be the sinusoidal mid-plane as shown.

equations:

$$\boldsymbol{\nabla} \cdot \boldsymbol{u} = 0, \tag{3.1}$$

$$\frac{\partial \boldsymbol{u}}{\partial t} + \boldsymbol{\nabla} \cdot (\boldsymbol{u}\boldsymbol{u}) = -\boldsymbol{\nabla} p + \nu \nabla^2 \boldsymbol{u} - \hat{\boldsymbol{e}}_x \Pi(t), \tag{3.2}$$

$$\frac{\partial \theta}{\partial t} + \boldsymbol{\nabla} \cdot (\boldsymbol{u}\theta) = \alpha \nabla^2 \theta - u \frac{\mathrm{d}\theta_w}{\mathrm{d}x}, \tag{3.3}$$

where the (kinematic) pressure gradient is decomposed into a periodic fluctuating component, $\boldsymbol{\nabla} p$, and a spatially uniform streamwise component, $\hat{\boldsymbol{e}}_x \Pi(t)$, with $\Pi < 0$ driving the flow at a constant mass flux. For temperature, we solve for the fluid temperature relative to the wall θ and drive heat transfer through a constant, prescribed wall-temperature gradient $\mathrm{d}\theta_w/\mathrm{d}x$. This forcing is equivalent to having a statistically uniform wall heat-flux (Kays & Crawford 1993) and is a common forcing strategy in channel-flow DNS of passive scalars (e.g. Kasagi, Tomita & Kuroda 1992; Kawamura *et al.* 1998; Alcántara-Ávila, Hoyas & Pérez-Quiles 2021).

The roughness considered is a 3-D sinusoidal roughness, given by

$$z_w(x, y) = k \cos(2\pi x/\lambda) \cos(2\pi y/\lambda), \tag{3.4}$$

where k is the sinusoidal semi-amplitude and the wavelength is fixed as $\lambda = 7.1k$ as in figure 5(*b*) for all the present cases, so that the roughness is geometrically similar. The surface has maxima and minima points at $z_w = \pm k$, which we presently refer to as roughness crests and troughs, respectively. This roughness has been investigated previously for both channels (Chung *et al.* 2015; MacDonald *et al.* 2016, 2019) and pipe flows (Chan *et al.* 2015, 2018). The computational domain has a channel half-height h, defined as the distance between the sinusoidal mid-plane and channel centreline, and the friction Reynolds number is defined on this height, $Re_\tau \equiv hU_\tau/\nu$. We measure the wall-normal direction z from the sinusoid midplane, although we will account for the virtual origin later in § 3.2. The domain is periodic in the streamwise and spanwise directions. No-slip impermeable ($\boldsymbol{u} = \boldsymbol{0}$) wall conditions and a zero fluid–wall temperature contrast ($\theta = 0$) are enforced using an immersed-boundary method (IBM). This code has been validated for momentum (Rouhi, Chung & Hutchins 2019) and has presently been extended to solve for rough-wall heat transfer. The IBM uses a direct-forcing approach

(Fadlun *et al.* 2000) with a volume-of-fluid interpolation. For spatial discretisation, the code employs the fully conservative fourth-order finite-difference scheme of Verstappen & Veldman (2003) for a staggered grid, while for time-stepping, we use the three-step Runge–Kutta method of Spalart, Moser & Rogers (1991). At each substep, the velocity field is projected onto a divergence-free space using the fractional-step algorithm (Perot 1993).

Mean quantities such as $U(z)$ for streamwise velocity or $\Theta(z)$ for temperature are defined to be the xyt-averages of their respective fields and for regions below the roughness, we take this average to be the intrinsic average. That is, the average that is representative of the volume occupied by the fluid domain (Nikora *et al.* 2007). Overbars (e.g. $\bar{u}$) will be used to denote time averages, while time-fluctuating fields will be denoted by a prime superscript: $u'(x, y, z, t) \equiv u(x, y, z, t) - \bar{u}(x, y, z)$.

Although we will focus our discussions primarily on the fully rough regime, our parameter space spans lower-transitional cases at $k^+ \approx 5.5$ towards the fully rough regime at $k^+ \approx 111$ for $Pr = 0.5$, 1.0 and 2.0, all detailed in table 1. Owing to our presently fixed $\lambda/k = 7.1$, the increasing k^+ will correspond to an increasing wall-unit-scaled roughness wavelength λ^+. These simulations employ minimal channels, whereby domain sizes $L_x \times L_y$ are truncated whilst still resolving the roughness sublayer (Chung *et al.* 2015; MacDonald *et al.* 2017), allowing for a parametric sweep at affordable cost. For each rough wall simulation, a smooth-wall simulation at matched Re_τ and domain size has also been conducted for a domain-size-independent measure of ΔU^+ and $\Delta\Theta^+$. Prescriptions for L_x and L_y follow from the recommendations of MacDonald *et al.* (2017). For minimal channels, the flow is explicitly captured in a region of 'healthy' turbulence up to a critical height $z_c \approx 0.4L_y$. We require that this healthy turbulence threshold resides above the roughness sublayer, above which the time-averaged flow is spatially homogeneous. For the same 3-D sinusoidal roughness in pipe flow, Chan *et al.* (2018) suggested that the roughness sublayer height could be estimated as $z_r \approx \lambda/2$ measured from the virtual origin. This estimate was based on an observation of the roughness-induced, dispersive motions becoming negligible at $z_r \approx \lambda/2$ universally for varying k^+ and λ/k (see Chan *et al.* 2018, figures 7*d* and 8*d*). The importance of in-plane roughness lengths in scaling z_r has been highlighted in the past, particularly for surfaces with strong in-plane heterogeneity (e.g. Raupach *et al.* 1991; Chung *et al.* 2021). Our present $\lambda/k = 7.1$ gives $z_r \approx \lambda/2 = 3.55k$, which is consistent with the common $z_r \approx 2k$–$5k$ estimate for rough-wall flows (e.g. Raupach *et al.* 1991; Jiménez 2004; Hong, Katz & Schultz 2011; Rouzes *et al.* 2019; Chung *et al.* 2021). To resolve the roughness sublayer flow with minimal channels, we then require $z_c = 0.4L_y > z_r \approx \lambda/2$ which can be satisfied with the spanwise domain length prescription $L_y \geq \max(100\nu/U_\tau, k/0.4, 2\lambda)$. The streamwise length prescription is $L_x \geq \max(3L_y, 1000\nu/U_\tau, \lambda)$ (MacDonald *et al.* 2017). In our present study, these constraints produce $L_x = 6\lambda$–$28\lambda \approx 2.4h$–$2.8h$, $L_y = 2\lambda$–$4\lambda \approx 0.39h$–$0.79h$ depending on the k^+ and h/k considered. This minimal channel approach was previously demonstrated by MacDonald *et al.* (2019) to adequately resolve the near-wall flow for temperature for a fixed $Pr = 0.7$ and employed even more restrictive computational domain sizes than our present study. For completeness, we have dedicated Appendix A towards further validating the minimal channel approach by comparing against full-span channel results for our varying $Pr = 0.5$, 1.0, 2.0, selecting $k^+ \approx 22$ as the candidate case. Our validation showed negligible differences between full-span and minimal channel results in the logarithmic flow region, consistent with other rough-wall minimal channel studies (e.g. MacDonald *et al.* 2017, 2019; Endrikat *et al.* 2021). We have selected $Re_\tau \approx 395$ as the lowest Reynolds number for our study, as this has been seen to

https://doi.org/10.1017/jfm.2023.125 Published online by Cambridge University Press

Re_τ	Pr	$\frac{h}{k}$	k^+	L_x^+	L_y^+	N_x	N_y	N_z	Δx^+	Δy^+	Δz_b^+	Δz_t^+	$\frac{\lambda}{\Delta x}$	$\frac{\lambda}{\Delta y}$	$\frac{k}{\Delta z_b}$	Δt^+	T_s	ΔU^+	$\Delta \Theta^+$
395	0.5	—	—	1091	156	128	32	300	8.52	4.87	0.34	5.70	—	—	—	0.25	1637	—	—
395	1.0	—	—	1091	156	128	32	300	8.52	4.87	0.34	5.70	—	—	—	0.25	1555	—	—
395	2.0	—	—	1091	156	192	64	440	5.68	2.43	0.23	3.89	—	—	—	0.16	215	—	—
395	0.5	72	5.5	1091	156	768	128	420	1.42	1.22	0.26	5.55	27	32	21	0.06	458	1.5	0.3
395	1.0	72	5.5	1091	156	768	128	420	1.42	1.22	0.26	5.55	27	32	21	0.06	331	1.5	0.8
395	2.0	72	5.5	1091	156	768	128	560	1.42	1.22	0.21	3.89	27	32	26	0.06	259	1.5	1.9
395	0.5	—	—	1013	156	128	32	300	7.91	4.87	0.34	5.70	—	—	—	0.25	1133	—	—
395	1.0	—	—	1013	156	128	32	300	7.91	4.87	0.34	5.70	—	—	—	0.25	842	—	—
395	2.0	—	—	1013	156	192	64	440	5.27	2.43	0.23	3.89	—	—	—	0.16	214	—	—
395	0.5	36	11	1013	156	384	64	520	2.64	2.43	0.26	5.45	30	32	43	0.09	283	4.1	1.2
395	1.0	36	11	1013	156	384	64	520	2.64	2.43	0.26	5.45	30	32	43	0.09	346	4.1	2.9
395	2.0	36	11	1013	156	384	64	640	2.64	2.43	0.23	3.96	30	32	47	0.08	360	4.0	6.3
395	0.5	—	—	1091	312	128	64	300	8.52	4.87	0.39	5.46	—	—	—	0.24	445	—	—
395	1.0	—	—	1091	312	128	64	300	8.52	4.87	0.39	5.46	—	—	—	0.24	351	—	—
395	2.0	—	—	1091	312	192	96	384	5.68	3.25	0.30	4.27	—	—	—	0.17	417	—	—
395	0.5	18	22	1091	312	192	64	660	5.68	4.87	0.28	5.54	27	32	77	0.07	181	6.7	2.0
395	1.0	18	22	1091	312	192	64	660	5.68	4.87	0.28	5.54	27	32	77	0.07	150	6.8	4.7
395	2.0	18	22	1091	312	192	64	660	4.26	2.43	0.24	3.76	37	64	90	0.06	62	6.9	8.9
590	0.5	—	—	1396	465	192	128	512	7.30	3.64	0.34	4.78	—	—	—	0.13	138	—	—
590	1.0	—	—	1396	465	192	128	512	7.30	3.64	0.34	4.78	—	—	—	0.14	100	—	—
590	2.0	—	—	1396	465	256	192	600	5.45	2.42	0.25	4.26	—	—	—	0.11	70	—	—
590	0.5	18	33	1396	465	324	108	920	4.31	4.31	0.29	6.34	54	54	111	0.03	37	8.0	2.6
590	1.0	18	33	1396	465	324	108	920	4.31	4.31	0.29	6.34	54	54	111	0.03	35	8.0	5.0
590	2.0	18	33	1396	465	456	152	1120	3.06	3.06	0.25	5.00	76	76	133	0.03	35	8.0	9.0
720	0.5	—	—	1704	568	192	128	500	8.88	4.44	0.43	5.97	—	—	—	0.08	59	—	—
720	1.0	—	—	1704	568	192	128	500	8.88	4.44	0.43	5.97	—	—	—	0.09	103	—	—
720	2.0	—	—	1704	568	256	192	700	6.66	2.96	0.22	4.64	—	—	—	0.10	97	—	—
720	0.5	18	40	1704	568	384	128	1180	4.44	4.44	0.29	5.59	64	64	137	0.03	40	8.4	2.7
720	1.0	18	40	1704	568	384	128	1180	4.44	4.44	0.29	5.59	64	64	137	0.03	39	8.6	5.2
720	2.0	18	40	1704	568	468	156	1360	3.64	3.64	0.25	5.12	78	78	163	0.02	29	8.5	9.1

Table 1. For caption see on next page.

https://doi.org/10.1017/jfm.2023.125 Published online by Cambridge University Press

Re_τ	Pr	$\frac{h}{k}$	k^+	L_x^+	L_y^+	N_x	N_y	N_z	Δx^+	Δy^+	Δz_b^+	Δz_t^+	$\frac{\lambda}{\Delta x}$	$\frac{\lambda}{\Delta y}$	$\frac{k}{\Delta z_b}$	Δt^+	T_s	ΔU^+	$\Delta\Theta^+$
1000	0.5	—	—	2367	789	256	192	660	9.20	4.10	0.45	6.29	—	—	—	0.12	63	—	—
1000	1.0	—	—	2367	789	256	192	660	9.20	4.10	0.45	6.29	—	—	—	0.13	126	—	—
1000	2.0	—	—	2367	789	384	256	900	6.16	3.08	0.24	5.01	—	—	—	0.08	40	—	—
1000	0.5	18	56	2367	789	576	192	1560	4.11	4.11	0.29	6.58	96	96	193	0.02	25	9.3	2.8
1000	1.0	18	56	2367	789	576	192	1560	4.11	4.11	0.29	6.58	96	96	193	0.02	27	9.6	5.2
1000	2.0	18	56	2367	789	512	384	1860	4.62	2.05	0.24	5.39	85	192	227	0.04	32	8.7	8.7
2000	0.5	—	—	4733	1578	512	384	1200	9.24	4.11	0.42	7.21	—	—	—	0.09	36	—	—
2000	1.0	—	—	4733	1578	512	384	1200	9.24	4.11	0.42	7.21	—	—	—	0.09	24	—	—
2000	2.0	—	—	4733	1578	768	512	1200	6.16	3.08	0.16	9.08	—	—	—	0.05	15	—	—
2000	0.5	18	111	4733	1578	1080	360	2700	4.38	4.38	0.29	10.6	180	180	386	0.02	8.9	10.9	2.8
2000	1.0	18	111	4733	1578	1080	360	2700	4.38	4.38	0.29	10.6	180	180	386	0.02	8.8	10.8	4.7
2000	2.0	18	111	4733	1578	1024	768	3200	4.62	2.05	0.25	8.58	171	384	450	0.03	13.6	11.0	7.1

Table 1. Table of runs for the (k^+, Pr) parameter sweep. The N_x, N_y and N_z are the number of grid points in the streamwise, spanwise and wall-normal directions, with uniform grid spacings Δx^+ and Δy^+, while the wall-normal grid spacing is given by the (constant) grid spacing below the roughness crests Δz_b^+ and the spacing at the channel centreline Δz_t^+. The average time step is given by $\Delta t^+ \equiv \Delta t U_\tau^2/\nu$ and $T_s \equiv TU_\tau/z_c$ is the total simulation time used for ensemble averaging based on z_c-sized eddy turnovers.

be sufficient for avoiding low-Re_τ influences from altering the logarithmic region (Chan *et al.* 2015; Thakkar, Busse & Sandham 2018). For a fixed k^+, these Re_τ influences may also be interpreted as the effect of the blockage ratio h/k on the logarithmic region since $Re_\tau = (h/k)k^+$. MacDonald *et al.* (2019) found that $Re_\tau \approx 395$ as their lowest Reynolds number did not alter near-wall heat transfer significantly for $Pr = 0.7$, concluding $Re_\tau \approx 395$ to be an adequate lower-bound. This same validation has been repeated in Appendix B for $Pr = 0.5, 1.0, 2.0$, where we similarly conclude the lower bounds $Re_\tau \gtrsim 395$, $h/k \gtrsim 18$ are adequate.

Uniform grid-spacing is employed in the streamwise and spanwise directions, while a hyperbolic grid stretching is used in the wall-normal direction above the roughness crests. Below this height, the grid spacing Δz_b in the wall-normal direction is uniform. Previous studies on the sinusoidal roughness we consider have determined that 24–48 cells per wavelength is adequate in resolving the roughness lateral scales (Chan *et al.* 2015, 2018; MacDonald *et al.* 2019; Rouhi *et al.* 2019). For higher-k^+ simulations, the limiting requirement on grid resolution shifts from resolving the roughness elements to resolving the smallest turbulence scales. We have kept the streamwise and spanwise grid spacings, $\Delta x^+ \lesssim 6$, $\Delta y^+ \lesssim 5$ for our $Pr = 0.5$ and $Pr = 1.0$ cases. For $Pr = 2.0$, the smaller scales in the temperature field will need to be captured by a finer resolution so the grid has been refined in these cases. We have conducted simulations at a constant Courant–Friedrichs–Lewy (CFL) number between 0.5 and 1, where the CFL number is defined presently by $\mathrm{CFL} \equiv \max_i(|u_i|\Delta t/\Delta x_i)$. Here, $|u_i|$ is the magnitude of the ith velocity component, Δx_i the grid spacing in the ith direction which determines the computational step size Δt. Time steps for the cases considered were typically limited by flow regions close to the wall for the wall-normal direction ($i = 3$), owing to the high computational grid density in this region, as well as observed increases in wall-normal velocities occurring close to the wall. The average time-step size, $\Delta t^+ \equiv \Delta t U_\tau^2/\nu$ is provided in table 1. Time-averaging windows are chosen based on sampling enough z_c-sized eddies in the log layer. These z_c-sized eddies have a characteristic time scale z_c/U_τ and the number of z_c/U_τ flow-through times is given by the simulation time $T_s \equiv TU_\tau/z_c$ in table 1. For the largest simulations at $k^+ \approx 111$, runtimes are limited to $T_s \approx 10$. Despite the limited sampling windows, the near-wall roughness sublayer flow and log-intercept measurements do not significantly vary, which is the focus of the present work. Details on statistical variations for our $k^+ \approx 111$ cases are reported in Appendix C.

3.2. *Virtual-origin effects*

To obtain robust measures of the logarithmic intercepts in (1.2*a*)–(1.2*d*), we need to measure from the virtual origin, by accounting for a shift, d (Raupach *et al.* 1991; Nikora *et al.* 2002; García-Mayoral, de Segura & Fairhall 2019). For low k^+, d represents a displacement of smooth-wall turbulence and can be obtained by shifting the Reynolds shear stress profiles to collapse with a smooth wall. We have adopted this approach to obtain d for our $k^+ = [5.5, 11, 22]$ cases and refer the reader to Endrikat *et al.* (2021, § 2.3) for details on the methodology.

At higher k^+, this framework may no longer hold, as the near-wall turbulent structures in the conventional, smooth-wall sense may no longer exist (Nikora *et al.* 2002; Jiménez 2004). Jackson (1981) proposed that d can be evaluated as the displacement which situates the centre of drag acting on the rough surface, although this definition may not always be appropriate (Cheng & Castro 2002; Coceal *et al.* 2007; Chung *et al.* 2021). The heat transfer analogue to Jackson's drag-centroid d, say, d_θ, would correspond to locating the centroid for the distribution of heat sources from the roughness elements

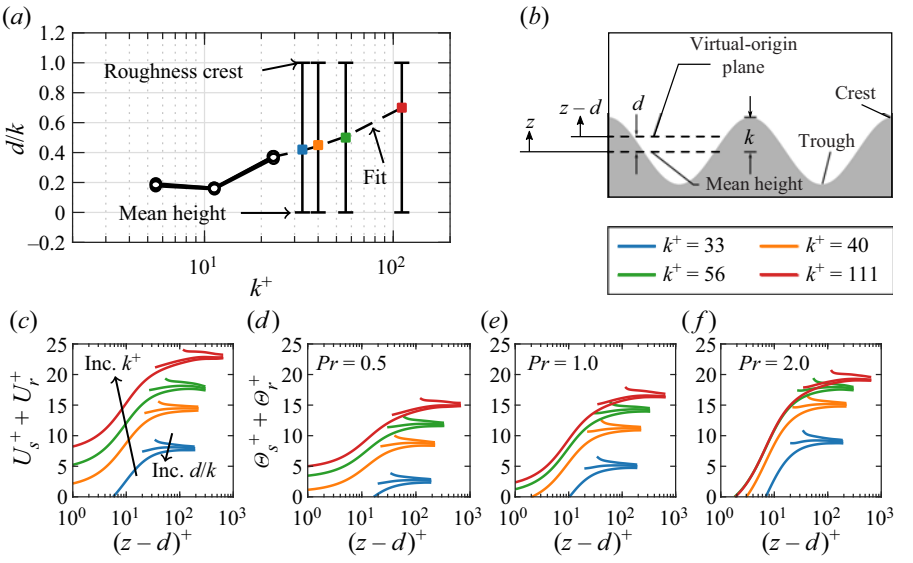

Figure 6. (*a*) Variation of d/k with respect to k^+. The circle markers designate the low-k^+ cases where d is evaluated as per Endrikat *et al.* (2021). Values for d/k (coloured markers) are obtained through an *ad hoc* fit for our higher-k^+ data: $d/k = -(k^+/365)^2 + (k^+/213) + 0.27$, which gives $d/k = \{0.42, 0.45, 0.50, 0.70\}$ for $k^+ = \{33, 40, 56, 111\}$. We select $d/k = [0, 1.0]$ (error bars) as bounds to assess the errors propagated by the uncertainty in d. (*b*) Schematic illustration of d and its relation to the roughness mean height and size k. (*c*) Velocity and (*d–f*) temperature difference profiles between smooth and rough walls from the roughness crests to the unphysical region z_c, the d/k fit in (*a*) and $d/k = 0, 1$. The profiles roughly collapse once z_c is approached and are staggered by $+3$ at each k^+ for clarity.

(Brutsaert 1982). Presently, we neglect this distinction, taking $d = d_\theta$, and instead elect to evaluate d for our $k^+ = [33, 40, 56, 111]$ cases through an *ad hoc* tuning to yield a close fit to $\kappa \approx 0.4$ and $\kappa_\theta \approx 0.46$ slopes in the logarithmic regions. Despite the *ad hoc* nature, we will show that the influence of the uncertainty in d is largely inconsequential when measuring the logarithmic intercepts. Figure 6(*a*) shows the d/k obtained from our *ad hoc* tuning approach. Alongside this, we have selected fixed prescriptions of $d/k = [0, 1]$ to assess the uncertainty this propagates into measurements of the logarithmic intercepts. The choices $d/k = 0,\ 1$ coincide with the extreme cases where the virtual origin is situated at the roughness mean and crest height, respectively, and are intended to be worst-case-scenario error measures for the uncertainty caused by d. As shown in the velocity and temperature difference profiles (figure 6*c–f*), variation in d/k produces slight changes in the difference profiles, but the profiles roughly collapse towards the same value as the unphysical region of minimal channels, z_c, is approached. In figure 7, we demonstrate that this d/k uncertainty does not significantly alter values for the logarithmic intercepts by presenting measurements of ΔU^+ and $\Delta\Theta^+$, obtained by evaluating the difference profiles (figure 6*c–f*) at the minimal channel critical height z_c, i.e. $\Delta U^+ = U_s^+(z_c^+) - U_r^+(z_c^+)$, $\Delta\Theta^+ = \Theta_s^+(z_c^+) - \Theta_r^+(z_c^+)$. We also examined the influence of measuring the roughness functions at different heights above the roughness sublayer, $z_r \approx \lambda/2$, and below z_c. This produced negligible variations in ΔU^+, $\Delta\Theta^+$ that were no greater than 0.3 (not shown). Figure 7(*a*) plots ΔU^+ at a fixed $d/k = 0$ and when fitted to the equivalent sand-grain roughness asymptote $\Delta U^+ = (1/0.4)\log(k_s^+) - 3.5$ yields $k_s/k \approx 3.3$. Prior studies on our present roughness in pipe flows have found $k_s/k \approx 4.1$ (Chan *et al.* 2015), which is also shown in figure 7(*a*) for reference. MacDonald

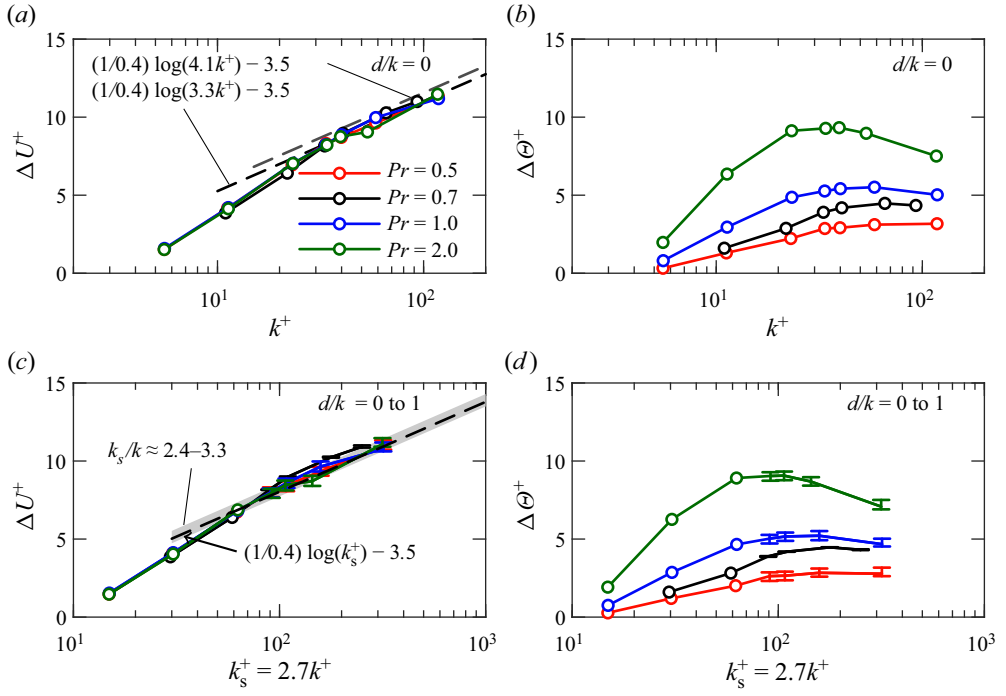

Figure 7. (*a*) ΔU^+ and (*b*) $\Delta\Theta^+$ measured with the mean roughness height ($d/k = 0$) as the origin. The $Pr = 0.7$ data are retrieved from MacDonald *et al.* (2019). (*c*,*d*) Roughness functions corrected for the virtual origin using the d/k fit in figure 6(*a*). The $k_s^+ = 2.7k^+$ prefactor for k^+ is obtained by collapsing the fully rough asymptote (dashed black line) of Nikuradse (1933). The error bars for high-k^+ data are evaluations for $d/k = 0$, 1 resulting in $k_s/k \approx 3.3$, 2.4, respectively.

et al. (2019) ascribed this k_s/k mismatch as being due to differences in blockage ratios ($h/k = 6.75$ as opposed to our present $h/k = 18$) and fundamental differences between pipes and channels. In figure 7(*c*,*d*), we propagate our d/k uncertainties into the error bars for ΔU^+, $\Delta\Theta^+$ when d/k is fixed as 0 and 1. The data of MacDonald *et al.* (2019) are included, taking into account virtual-origin effects using our fit in figure 6(*a*). Their data tend to produce smaller error bars, which is due to a different prescription for z_c^+ where the roughness functions are measured. The d/k uncertainty results in $k_s/k \approx 2.4$–3.3, with $k_s/k \approx 2.7$ as the result from our d/k fit (figure 6*a*). The consequent uncertainties in ΔU^+ caused by d/k variations result in relative errors no greater than 7.5 %, which are not too significant bearing in mind this considers the worst-case-scenario limits of $d/k = 0$ and 1. Later in § 4.2 when we present mean profiles, we will provide further evidence demonstrating the insensitivity of the high-k^+ data with respect to choices in d.

The $\Delta\Theta^+$ trends suggested by figure 7(*b*,*d*) are that heat transfer augmentation through roughness is most significant for higher-Pr fluids. Across all Pr, $\Delta\Theta^+$ appears to plateau in the vicinity of $k^+ \approx 40$, before beginning a gradual decrease, with signs that this peak occurs at lower k^+ for higher Pr. It is unclear whether this decrease should continue or if there exists another asymptotic scaling for $\Delta\Theta^+$. A continual decrease in $\Delta\Theta^+$ for increasing k^+ would imply that $\Delta\Theta^+$ would eventually attain a negative value. That is, a reduction in heat transfer relative to a smooth wall which seems unintuitive. Ultimately however, higher-k^+ data are needed to affirm the asymptotic state of $\Delta\Theta^+$ for $k^+ \to \infty$.

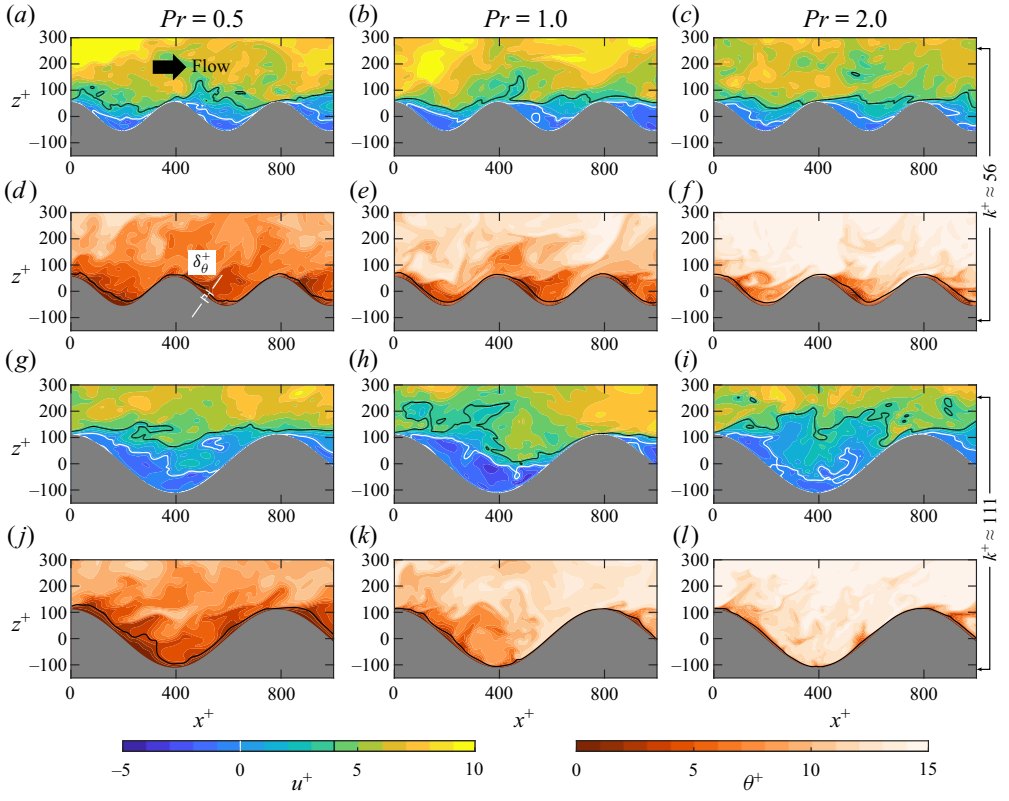

Figure 8. (*a–c*) Instantaneous streamwise velocity fields at $k^+ = 56$ with contour lines at $u^+ = 0$, 4 (white, black) to highlight stagnant fluid regions and the slip velocity across the roughness crests, respectively. The corresponding temperature fields are shown in (*d–f*) for $Pr = 0.5$–2.0 where the black contour lines show coordinate traces of δ_θ^+, obtained by projecting the distance δ_θ^+ in the local wall-normal direction (illustrated in *d*). The local δ_θ^+ is estimated as the departure from a locally fitted linear tangent by a threshold of 10 % relative error. Refer to the body text for more details. (*g–l*) Same as (*a–f*) for $k^+ = 111$.

4. Fully rough phenomenology

4.1. *Flow visualisations*

In figure 8, we provide instantaneous views of the flow fields close to the wall at our two highest $k^+ = 56$, 111, visualising the streamwise velocity u^+ as well as spatial variations of the conductive sublayer, δ_θ^+ in the temperature fields. Recall that δ_θ^+ represents the extent of the local region in which the temperature varies linearly. To obtain rough estimates of δ_θ^+ in figure 8, we have first selected a temperature threshold value, $\theta^+ = 2Pr$ that was found to lie within the linear conductive regions at a wide range of spatial locations for all the cases shown in figure 8. A local tangent was then fitted to the wall-normal temperature profile at each wall location which passed through the location of this threshold coordinate. We then take δ_θ^+ to be the point at which the wall-normal temperature departs from this tangent by a 10 % relative error, such that it roughly encapsulates the extent of the linear region. At both $k^+ = 56$, 111, we can make three distinct observations concerning the spatial variations of δ_θ^+ in the temperature fields (figure 8*d–f*,*j–l*). First, the thicker conductive sublayers observed at lower-*Pr* is reflective of the tendency for conduction to occur over greater distances in lower-*Pr* fluids (Kays & Crawford 1993; Dimotakis 2005). Second, the

thinnest regions of δ_θ^+ are typically seen in exposed, windward locations – a phenomena which relates to the higher heat transfer that is typically observed due to impingement of windward faces (Peeters & Sandham 2019), as a higher heat transfer corresponds to a thinner observed conductive sublayer. Third, the observation of detaching plumes, corresponding to relatively thick regions of δ_θ^+ tend to emerge in sheltered, leeward regions. The formation of these plumes roughly correlate to regions of turbulent reversed flow, $u^+ < 0$, as seen in the velocity fields (figure 8*a–c*,*g–i*). The primary difference in the $k^+ = 111$ fields from $k^+ = 56$ appears to be that the detaching plumes diminish in size relative to the roughness size k. The visualisations show that the reversed-flow regions cover the majority of the surface wetted area and thereby is the primary flow acting to mix temperature locally. This prominence of reversed-flow however, does not preclude the existence of other mechanisms which may drive heat transfer locally. Highlighted by the velocity contour lines $u^+ = 4$ in figure 8, regions such as crests are exposed to faster flow producing higher shear, which may suggest a Reynolds-analogy-type shear-driven heat transfer mechanism not unlike a smooth-wall boundary layer that is postulated in the phenomenology of § 2.3. A similar smooth-wall analogy at exposed regions was discussed by Chan-Braun, García-Villalba & Uhlmann (2011) for transitionally rough flow over packed spheres which motivated them to adopt a smooth-wall analogy model for predicting the hydrodynamic drag. When considering these packed spheres in the fully rough regime however, Mazzuoli & Uhlmann (2017) found that the success of the smooth-wall analogy model diminishes, which they attributed to the absence of any smooth-wall-type flow structure near the wall. We will dedicate § 4.3 to scrutinising the validity of a local smooth-wall, Reynolds-analogy-type behaviour in the fully rough regime.

4.2. *Mean quantities and scaling laws*

Before examining hypothesised local phenomena associated with fully rough heat transfer, we will look at features of the mean flow that are pertinent to the phenomenologies outlined in § 2. One such feature is the notion of the temperature being well mixed below z_i by the scale-separated turbulent eddies, with significant variations only occurring in the conductive sublayer very close to the surface. We first test this assumption in figure 9(*a–d*) against the mean profiles. The near-wall distributions of Θ^+ at higher-k^+ tend to support this hypothesis, as Θ^+ is held approximately uniform below the logarithmic region (the lower limit of the logarithmic region, z_i, is marked with the open symbols). The velocity profiles (figure 9*a*), however, do not seem to exhibit this same degree of well mixing. Note that the profiles in figure 9(*a–d*) only show data up to the minimal channel unphysical region, $(z-d)^+ = z_c^+ = 0.4L_y^+$. For our $k^+ \geq 22$ cases, this is fixed at $z_c/h \approx 0.32$, which lies above the conventionally quoted extent of the logarithmic region, $z/h \approx 0.15$ (e.g. Pope 2000; Marusic & Monty 2019). Given that our present work is not concerned with the outer-scale flow dynamics and that the wake region beyond z_c is inherently unphysical in minimal channels, the data beyond z_c are not of importance here. Figure 9(*e–l*) examines further evidence by highlighting the mean profile distributions within the roughness canopies against logarithmic and linear z/k axes. For increasing k^+, we observe the gradual emergence of a steeper temperature gradient beginning at the roughness troughs, $z/k = -1$, best seen on the linear z/k axes (figure 9*j–l*). At our highest $k^+ = 111$, this sharp increase accounts for nearly 50 % of the total temperature variation in the channel, lending credence to the assumption of well-mixing. For the velocity in figure 9(*e*), we highlight the fully rough behaviour, $U^+ = (1/\kappa)\log[(z-d)/k] + C$, where $C \approx 6.0$ corresponds to our choice of d/k in figure 9(*a*) consistent with $k_s/k \approx 2.7$. The bounds for $d/k = [0, 1]$ (dashed red lines) show that despite being representative of extreme cases

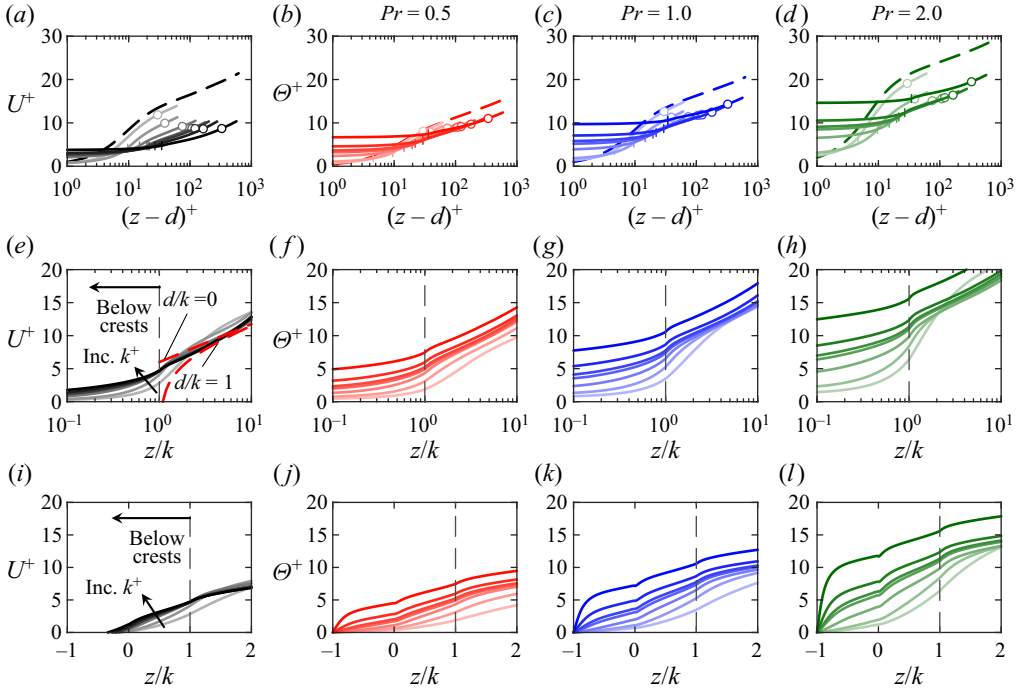

Figure 9. (*a–d*) Intrinsically averaged velocity and temperature profiles for $k^+ \approx 5.5$–111, where darker lines correspond to increasing k^+. The circle markers locate estimates for the beginning of the logarithmic region, $z_i^+ = \max(30, z_r^+)$, where $z_r^+ \approx \lambda^+/2 = 3.55k^+$ is the roughness sublayer height (Chan *et al.* 2018) and the vertical lines mark the roughness crests, $z/k = 1$. The dashed lines show the smooth wall profile at $Re_\tau \approx 2000$. Only data below $(z-d)^+ = z_c^+$ are shown. (*e–h*) Intrinsically averaged profiles versus z/k log-axes and (*i–l*) linear-axes highlighting the distributions within the roughness canopies ($z/k \leq 1$). The dashed red lines in (*e*) demonstrate the insensitivity of high-k^+ trends with respect to the choice in d/k by plotting $U^+ = (1/\kappa)\log[(z-d)/k] + C$, for $d/k = [0, 1]$, where $C \approx 6.0$ is obtained from our $k_s/k = 2.7$ result (figure 7*c*).

for the uncertainty in d, this amounts to an inconsequential uncertainty in the logarithmic intercept as the lines eventually collapse above $z/k \approx 3$. The mean temperature profiles against $\log(z/k)$ meanwhile (figure 9*f–h*), do not show a single fully rough asymptote like the velocity, instead showing a persistent dependence on k^+.

Recall from § 2, the fully rough phenomenologies are distilled into a scaling law for the temperature at the beginning of the logarithmic region $\Theta^+(z - d = z_i) \equiv \Theta_i^+ \sim (k^+)^p Pr^m$. The exponents p and m will now be investigated. To obtain self-consistent measures of the various logarithmic intercepts in (1.1) and (1.2), we have performed regression fits to the logarithmic mean profiles in figure 9(*a–d*). For evaluation of Θ_i^+, we have adopted the prescription $z_i^+ = \max(30, z_r^+)$, where $z_r^+ \approx \lambda^+/2 = 3.55k^+$ is the roughness sublayer thickness (Chan *et al.* 2018). The condition $z_i^+ = z_r^+$ sets the beginning of the log layer to coincide with the end of the roughness sublayer and, as seen in figure 9(*a–d*), provides a reasonable estimate at higher k^+. For lower k^+, the flow retains a form similar to that of a smooth wall, with the roughness sublayer lying below the logarithmic region (Luchini 1996). For these instances, we set $z_i^+ = 30$, which coincides with the typical interfacial height expected from a smooth-wall flow (Brutsaert 1982).

The $\Theta_i^+ \sim (k^+)^p$ scaling is assessed directly in figure 10(*a*). As the fully rough regime is approached, our present data support the $\Theta_i^+ \sim (k^+)^{1/4}$ scaling of Brutsaert (1975*b*),

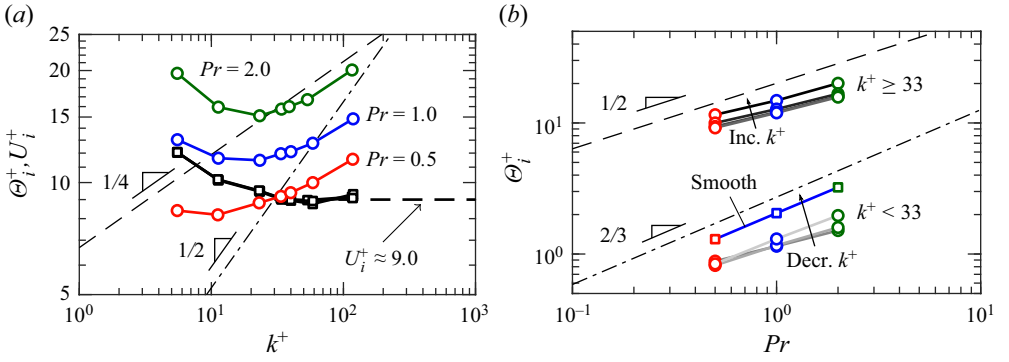

Figure 10. (*a*) Scaling of the interfacial temperature $\Theta_i^+ \equiv \Theta^+(z - d = z_i)$, where $z_i^+ = \max(30, \lambda^+/2)$, which shows an approach to $\Theta_i^+ \sim (k^+)^{1/4}$ rather than $\Theta_i^+ \sim (k^+)^{1/2}$ in the fully rough regime. The interfacial velocity, $U_i^+ \equiv U^+(z - d = z_i)$ (black squares), by contrast, shows an approach to a constant $U_i^+ \approx 9.0$. (*b*) The scaling of Θ_i^+ with respect to Pr, where solid lines join data at matched k^+ which increase in darkness with k^+. This shows that high-k^+ tend to follow a $\Theta_i^+ \sim Pr^{1/2}$ scaling, whilst at lower k^+, the smooth-wall $\Theta_i^+ \sim Pr^{2/3}$ scaling is more closely followed. For the trends to be discernible, data for $k^+ < 33$ have been staggered down a decade, $0.1\Theta_i^+$, while the smooth wall data (square markers; blue line) show $0.15\Theta_i^+$.

while the $\Theta_i^+ \sim (k^+)^{1/2}$ scaling does not appear to be followed along any k^+ range. The failure of this scaling despite its contemporary support (Li *et al.* 2017, 2020) will be treated specifically in §4.3. This continual increase in Θ_i^+ with k^+ stands in contrast with what is understood in the interfacial velocity, $U_i^+ \equiv U^+(z - d = z_i)$. As seen in figure 10(*a*), unlike with Θ_i^+, a constant value $U_i^+ \approx 9.0$ is attained. In figure 10(*b*), the $\Theta_i^+ \sim Pr^m$ scaling is assessed. With increasing k^+, our data appear to be in reasonable agreement with the $m = 1/2$ scaling of Brutsaert (1975*b*). In addition, the $\Theta_i^+ \sim Pr^{2/3}$ smooth-wall scaling (Kader 1981; Brutsaert 1982; Durbin & Pettersson-Reif 2011) is included, which is approached for small k^+. Owing to the success of both the $p = 1/4$ and $m = 1/2$ scalings, we see that plotting the $\Theta_i^+ \sim (k^+)^{1/4} Pr^{1/2}$ relation in figure 11(*a*) is able to collapse our $k^+ > 22$ data across all Prandtl numbers onto a single curve, $\Theta_i^+ = 3.7(k^+)^{1/4} Pr^{1/2} + 2.6$, where the constants depend only on roughness geometry. This suggests that one needs to only find the constants for a single working fluid, i.e. a single Pr, and that the prediction may be generalised to arbitrary $Pr > 1$.

Although the data of figure 11(*a*) are presented in terms of Θ_i^+ and k^+, the data can also be expressed using the roughness length z_0 or equivalent sand-grain roughness k_s. For example, we can obtain the inverse roughness Stanton number $St_k^{-1} \equiv \Theta^+(z_0^+) = (1/\kappa_\theta)\log(z_0/z_i) + \Theta_i^+$ by combining (1.2*b*) with (1.2*d*). Since $z_0 \propto z_i \propto k$ in the fully rough regime (Brutsaert 1982), this amounts to $St_k^{-1} \sim \Theta_i^+ \sim (k^+)^{1/4} Pr^{1/2} \sim (z_0^+)^{1/4} Pr^{1/2}$, as is corroborated in figure 11(*b*). For completeness, the set of expressions equivalent to the $\Theta_i^+ = 3.7(k^+)^{1/4} Pr^{1/2} + 2.6$ result we find in figure 11(*a*) are

$$St_k^{-1}(z_0^+, Pr) = (1/\kappa_\theta)\log(z_0/z_i) + 3.7(k/z_0)^{1/4}(z_0^+)^{1/4} Pr^{1/2} + 2.6, \tag{4.1a}$$

$$g(k_s^+, Pr) = (1/\kappa_\theta)\log(k_s/z_i) + 3.7(k/k_s)^{1/4}(k_s^+)^{1/4} Pr^{1/2} + 2.6, \tag{4.1b}$$

$$\Delta\Theta^+(k^+, Pr) = (1/\kappa_\theta)\log[(z_i/k)k^+] + A_\theta - 3.7(k^+)^{1/4} Pr^{1/2} - 2.6, \tag{4.1c}$$

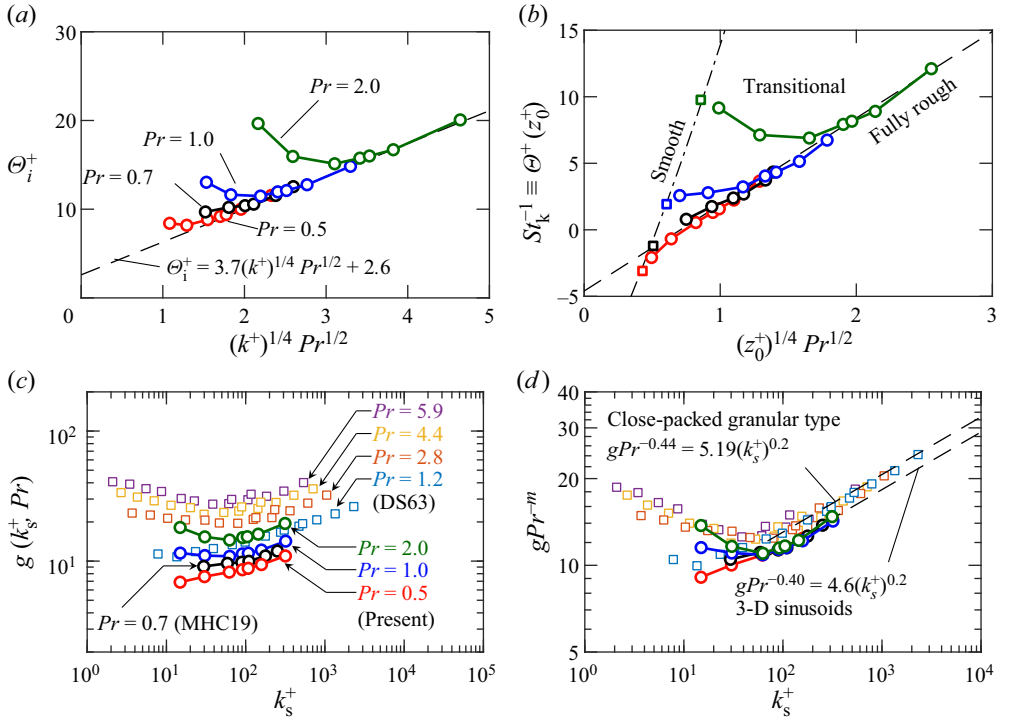

Figure 11. (*a*) Interfacial temperature with respect to the $p = 1/4$, $m = 1/2$ power-law scaling of Brutsaert (1975*b*) which predicts the high-k^+ DNS data. (*b*) The same information in (*a*) reformulated using z_0^+ and the roughness Stanton number, St_k. For smooth walls, $St_k^{-1} = c_\theta Pr^{2/3} + (1/\kappa_\theta)\log[0.135/(c_\theta Pr^{-1/3})]$, deduced from the intersection of the conductive and logarithmic regions, where $c_\theta \approx 11.7$ presently. For fully rough, $St_k^{-1} = 6.5(z_0^+)^{1/4}Pr^{1/2} - 4.6$ (see (4.1*a*)). The $Pr = 0.7$ data are processed from MacDonald *et al.* (2019). (*c*,*d*) Log-intercept $g(k_s^+, Pr)$ comparing the present $Pr = 0.5$–2.0 sinusoidal roughness and the $Pr = 1.2$–5.9 close-packed granular type roughness of Dipprey & Sabersky (1963), with empirical fits given in (*d*).

where $z_0/z_i \approx 0.03$, $k/z_0 \approx 11$, $k/z_i = 1/3.55 = 0.28$ and $k_s/z_i \approx 0.76$ are self-consistent constants in the fully rough regime for our present roughness. In figure 11(*b*), we also include the smooth-wall asymptote, $\Theta^+(z_0^+) = (1/\kappa_\theta)\log(z_0^+) + A_\theta$, where $z_0^+ = \exp(\kappa A) \approx 0.135$ from combining (1.1*a*) and (1.1*b*), and $A_\theta = c_\theta Pr^{2/3} - (1/\kappa_\theta)\log(c_\theta Pr^{-1/3})$, where $c_\theta \approx 11.7$ presently. This A_θ form is deduced from the intersection of the conductive and logarithmic regions (e.g. Kader 1981; Kays & Crawford 1993; Durbin & Pettersson-Reif 2011) and is commonly approximated by $A_\theta = aPr^{2/3} - b$, where a and b are constants (cf. Brutsaert 1982, table 4.1). Figure 11(*b*) then provides an overall view for rough-wall heat transfer, from smooth to fully rough under a variety of working fluids.

In figure 11(*c*,*d*), we show comparisons of our present sinusoidal surface with experimental data on close-packed granular type roughness from Dipprey & Sabersky (1963) spanning $Pr = 1.2$–5.9 adopting the g-function formulation (1.2*c*). We remark how their data tend to exhibit similar qualitative behaviour to our present sinusoidal surface: a minimum at $k_s^+ \approx 70$, followed by the power-law dependence $g \sim (k_s^+)^p Pr^m$ in the fully rough regime. Their empirically fitted exponents, $p = 0.20$, $m = 0.44$ are similar to the proposals $p = 1/4$, $m = 1/2$ of Brutsaert (1975*b*). Fixing $p = 0.20$, as done by Dipprey &

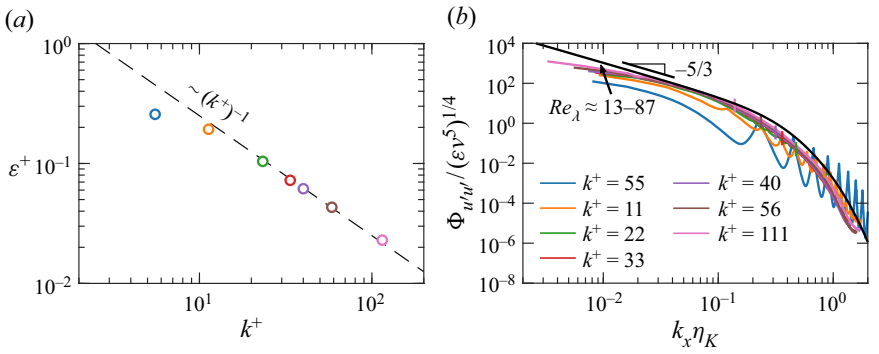

Figure 12. (*a*) Turbulent dissipation rate $\varepsilon \equiv 2\nu\overline{s'_{ij}s'_{ij}}$ computed approximately $0.3\nu/U_\tau$ above the roughness crests, compared against $\varepsilon^+ \sim (k^+)^{-1}$ (dashed line) which in dimensional form is the $\varepsilon \sim U_\tau^3/k$ approximation. (*b*) Streamwise energy spectra at the same z-location, normalised on Kolmogorov units. The vertical lines mark the roughness size k and the black line adopts the model spectrum of Pope (2000) for the dissipation range, $\Phi(K) = C_k\varepsilon^{2/3}K^{-5/3}\exp\{-\beta\{[(K\eta_K)^4 + c_\eta^4]^{1/4} - c_\eta\}\}$, $\Phi_{u'u'}(k_x) = \int_{k_x}^{\infty} K^{-1}\Phi(K)(1 - k_x^2/K^2)\,\mathrm{d}K$ with $C_k \approx 1.5$, $\beta \approx 5.2$ and $c_\eta \approx 0.4$. The range of Taylor Reynolds numbers, Re_λ computed above the roughness crests is also provided.

Sabersky (1963), we find a similar value of $m = 0.40$ that collapses our present data well (figure 11*d*).

A key ingredient to the Kolmogorov–Brutsaert phenomenology concerns the energy cascade from scales $z_i \propto k$ to the Kolmogorov scale η_K, characterised by its constant turbulent dissipation rate $\varepsilon \sim U_\tau^3/(\kappa k)$ in the well-mixed region (cf. figure 3*a*), which in dimensionless form is $\varepsilon^+ \sim (\kappa k^+)^{-1}$. In figure 12(*a*), we compare this scaling against measurements of ε approximately $0.3\nu/U_\tau$ above the roughness crests, which we presently compute as $\varepsilon \equiv 2\nu\overline{s'_{ij}s'_{ij}}$, where $s'_{ij} \equiv (1/2)(\partial u'_i/\partial x_j + \partial u'_j/\partial x_i)$ is the fluctuating rate-of-strain tensor (Pope 2000). The scaling is in good agreement with our present data, even appearing to hold at intermediate values of k^+ in the transitional regime, $k^+ \approx 22$. This could explain the success of Brutsaert's scaling in figure 11(*a*) at intermediate values of k^+.

Another view of this cascade is provided by figure 12(*b*) in streamwise energy spectra with respect to the streamwise wavenumber, $\Phi_{u'u'}(k_x)$, computed at the same z-location in figure 12(*a*), serving to illustrate the energy distribution across spatial scales and is related to the Reynolds stress as $\overline{u'u'} \equiv \int_0^\infty \Phi_{u'u'}\,\mathrm{d}k_x$. Note that k_x here is the streamwise wavenumber, not to be confused with the roughness length scale, and that u' is defined as the deviation from the time-average mean: $u'(x, y, z, t) \equiv u(x, y, z, t) - \bar{u}(x, y, z)$. The $\Phi_{u'u'}$ spectra show oscillatory peaks corresponding to harmonics of the roughness wavelength λ/n for some integer n, and are more pronounced for low-k^+. Physically, these oscillations can be interpreted as the roughness topography creating motions near the wall with characteristic length scales $O(\lambda)$. Wall-parallel visualisations of velocity fluctuations at matched z-locations to the $\Phi_{u'u'}$ spectra in figure 12(*b*) (not shown) were found to be consistent with this intuition, with imprints of the roughness topography visible in the form of small wakes coincident with roughness crests. These were most pronounced for low-k^+, much like the peaks of $\Phi_{u'u'}$ appearing strongest for low-k^+. Likewise, results of surface features being visible in the turbulent fluctuations have been observed previously (e.g. Abderrahaman-Elena, Fairhall & García-Mayoral 2019; Fairhall, Abderrahaman-Elena & García-Mayoral 2019). It appears that the $k^+ \geqslant 22$ cases, where

$\varepsilon^+ \sim (k^+)^{-1}$ holds (figure 12*a*), display spectra which exhibit roughly universal behaviour at wavenumbers $k_x\eta_K > 10^{-2}$. Conventional understanding of turbulence argues that the inertial subrange down to the dissipation range becomes a universal function of $k_x\eta_K$ once an energy-cascade has developed through sufficient scale separation (Tennekes & Lumley 1972; Pope 2000). The model spectrum (figure 12*b*, black line) of Pope (2000), which relies on this intuition, is closely followed by our $k^+ \geq 22$ spectra, supporting the view of Brutsaert (1975*b*) in an energy-cascade having developed in the vicinity of the roughness elements. For reference, we also compute the Taylor Reynolds number above the roughness crests, $Re_\lambda \equiv u_{rms}\lambda_T/\nu$, where $\lambda_T \equiv u_{rms}(15\nu/\varepsilon)^{1/2}$ is the Taylor microscale and u_{rms} is the root mean square streamwise velocity (Pope 2000). Our present data cover a range $Re_\lambda \approx 13$–87 for $k^+ \approx 5.5$–111, and, for the $k^+ \geqslant 22$ cases which collapse in figure 12(*b*), cover $Re_\lambda \approx 44$–87. These magnitudes are similar to published data where a $k_x^{-5/3}$ scaling in the inertial subrange is weakly present (e.g. Saddoughi & Veeravalli 1994; Dimotakis 2000; Donzis & Sreenivasan 2010), which appears consistent with our data.

4.3. *Local roughness crest scaling*

As was seen in figure 10(*a*), from a spatially averaged view, the $p = 1/2$ exponent from the Prandtl–Blasius phenomenology is seen to fail in favour to the Kolmogorov–Brutsaert $p = 1/4$ exponent for $\Theta_i^+ \sim St_k^{-1} \sim (k^+)^p$. Whilst the failure of the $p = 1/2$ in § 2.3 scaling may imply that the laminar boundary-layer phenomenology of Prandtl–Blasius is inappropriate for rough walls, we will demonstrate that such a phenomenology can be apt when we examine the flow locally at roughness crests. Here, the intuition which motivates this insight comes from the observation that roughness crests, being regions where the flow remains attached and is exposed to higher shear (cf. velocity in figure 8) are regions where we may expect the flow to be most analogous to a shear-driven, Prandtl–Blasius-type boundary layer.

In figure 13(*a*,*b*), we show time-averaged wall-normal velocity and temperature ($Pr = 1.0$) profiles taken at roughness crests. The axes are scaled on the locally measured viscous friction velocity at the crest, $u_* \equiv \sqrt{|\tau_v|/\rho}$, where $\tau_v/\rho \equiv \partial u/\partial n|_w$ and local friction temperature $\theta_* \equiv q_w/(\rho c_p u_*)$. Here, we observe clear linear viscous–conductive regions, $u^*_{crest} = z^*_{crest}$ and $\theta^*_{crest} = Prz^*_{crest}$, with the extent of these regions corresponding to the local viscous and conductive sublayer thicknesses, δ_ν and δ_θ, respectively. These thicknesses are located through the minima of second derivatives: $\mathrm{d}^2u_{crest}/\mathrm{d}z^2$ and $\mathrm{d}^2\theta_{crest}/\mathrm{d}z^2$ (figure 13*a*,*b*, markers). The insets of figure 13(*a*,*b*) show that these measures of δ_ν and δ_θ are indeed appropriate to scale u_{crest} and θ_{crest} in the linear viscous–conductive regions for $k^+ \gtrsim 22$.

The advantage in introducing these viscous–conductive quantities defined by the second derivative minima is that they can be computed unambiguously in smooth-wall DNS and are defined for Prandtl–Blasius boundary layers (cf. figure 4*c*), enabling direct comparison. Specifically, we may define a primitively scaled skin-friction coefficient, $\widehat{C_f}$, Stanton number, $\widehat{St}$, as well as a viscous Reynolds number, Re_{δ_ν}:

$$\frac{\widehat{C_f}}{2} \equiv \frac{\tau_\nu}{\rho u_{\delta_\nu}^2}, \quad \widehat{St} \equiv \frac{q_w}{\rho c_p u_{\delta_\nu}\theta_{\delta_\theta}}, \quad Re_{\delta_\nu} \equiv \frac{u_{\delta_\nu}\delta_\nu}{\nu}. \tag{4.2a–c}$$

Here, we use primitive scaling to refer to normalisations on the basic viscous–conductive quantities of the flow, such that one can define and compare the quantities in (4.2)

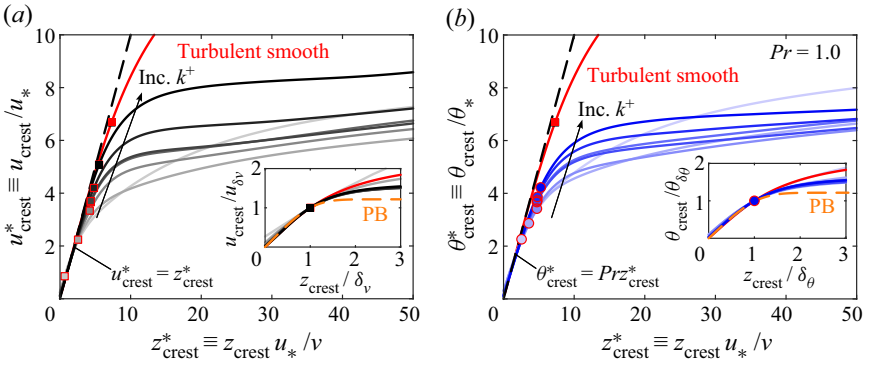

Figure 13. (*a*) Time- and phase-averaged velocity profiles at crest locations scaled by the local viscous friction velocity $u_* \equiv \sqrt{|\tau_\nu|/\rho}$ with increasing line darkness with k^+. Here, z_{crest} measures the wall-normal distance taking roughness crests (cf. figure 6*b*) as the origin. The markers locate the local viscous sublayer thickness, δ_ν, situated by the local minima of $\mathrm{d}^2u_{crest}/\mathrm{d}z^2$, and velocity at this location u_{δ_ν} for each k^+ (the marker fill colours match the mean profile colours). A turbulent smooth-wall profile ($Re_\tau \approx 2000$, red line) is included to illustrate the gradual approach to local smooth-wall conditions with increasing k^+. (*b*) Same as (*a*) but for temperature at $Pr = 1.0$, scaled on the local friction temperature $\theta_* \equiv q_w/(\rho c_p u_*)$. The markers locate the local conductive sublayer, δ_θ (corresponding to $\mathrm{d}^2\theta_{crest}/\mathrm{d}z^2$ minima locations) and the temperature at these locations, θ_{δ_θ}. The insets of (*a*,*b*) demonstrate that re-scaling the profiles on viscous–conductive quantities, $(\delta_\nu, u_{\delta_\nu})$, $(\delta_\theta, \theta_{\delta_\theta})$, collapses the profiles and agree near the wall with the Prandtl–Blasius (PB) profiles.

between the different flow configurations (e.g. smooth wall versus roughness crest). In the case of Prandtl–Blasius boundary layers, one has that $\widehat{St}Pr^{2/3} \propto \widehat{C}_f \sim Re_{\delta_\nu}^{-1}$ (Schlichting & Gersten 2017), coinciding with the Reynolds analogy (Bird *et al.* 2007). In figure 14(*a*,*b*), we test these scalings directly, while also comparing with the values obtained from a smooth-wall DNS ($Re_\tau \approx 2000$) to illustrate the approach to smooth-wall-like conditions locally. The primitively scaled quantities for smooth walls did not change with Re_τ, so we have elected to only show smooth-wall data for a single Re_τ in figure 14 for clarity. Our empirical fits, $\widehat{C}_f/2 = 1.9Re_{\delta_\nu}^{-1.17}$, $\widehat{St}Pr^{0.75} = 0.72Re_{\delta_\nu}^{-0.82}$ are similar to the theoretical $Re_{\delta_\nu}^{-1}$, $Pr^{2/3}$ exponents, providing supporting evidence for a Prandtl–Blasius-like behaviour at crests. The mismatch in the Reynolds number exponent between skin-friction and heat transfer $\widehat{C}_f \sim Re_{\delta_\nu}^{-1.17}$, $\widehat{St} \sim Re_{\delta_\nu}^{-0.82}$ is perhaps indicative of crest regions not being driven purely by a Reynolds-analogy-type mechanism. The compensated viscous-to-conductive sublayer ratio $(\delta_\theta/\delta_\nu)Pr^{1-2/3}$ (figure 14*c*), too, shows a mild departure from the Reynolds analogy limit of $(\delta_\theta/\delta_\nu)Pr^{1-2/3} = \text{constant}$, with instead a weak dependence on Re_{δ_ν}. Further assumptions in the rough-wall Prandtl–Blasius theory are tested in figure 14(*d*), where we examine the generalisation of the roughness length scale as an effective streamwise fetch for the local flow: $x \propto k$. Following our discussion surrounding (2.7*a*,*b*), this assumption led to the canonical $\delta_\nu/x \sim Re_x^{-1/2}$ of Prandtl–Blasius theory being modified to $\delta_\nu/k \sim Re_k^{-1/2}$, where $Re_k \equiv u_{\delta_\nu}k/\nu$. As seen in figure 14(*d*), measurements at the crests agree well with this prediction: $\delta_\nu/k = 1.38Re_k^{-0.50}$ for $k^+ \gtrsim 33$, thus supporting the local Prandtl–Blasius boundary-layer arguments put forward by Owen & Thomson (1963) and Yaglom & Kader (1974) in § 2.3.

Next, we discuss the approach to smooth-wall-like behaviour at crests in the context of the smooth-wall DNS datapoints shown in figure 14(*a–c*). Here, the smooth wall

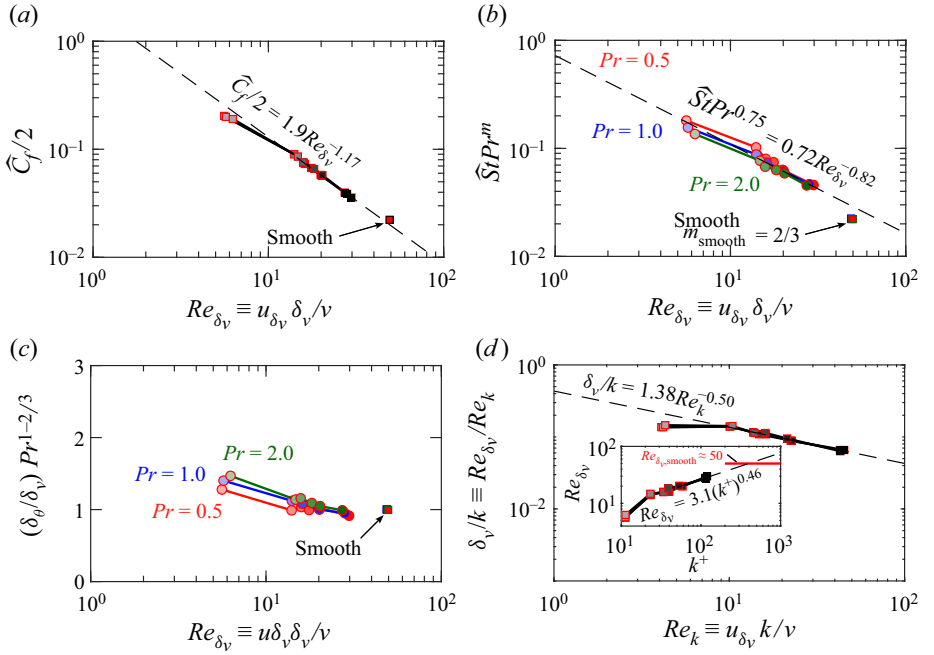

Figure 14. Empirical scalings measured at roughness crests for $k^+ > 11$ showing (*a*) the viscous skin-friction coefficient normalised on primitive, viscous quantities, $\widehat{C}_f/2 \equiv \tau_v/(\rho u_{\delta_\nu}^2)$. The value computed from a smooth wall DNS ($Re_\tau \approx 2000$) is also included. (*b*) Same as (*a*) for a Stanton number normalised on viscous–conductive quantities: $\widehat{St} \equiv q_w/(\rho c_p u_{\delta_\nu\theta_{\delta_\theta}})$. (*c*) Compensated ratio between local conductive and viscous sublayer thicknesses $(\delta_\theta/\delta_\nu)Pr^{1-2/3}$, which show a mild dependence on Re_{δ_ν}. (*d*) Scaling of $\delta_\nu/k \equiv Re_{\delta_\nu}/Re_k$ with respect to Re_k, which agrees with the theoretical $Re_k^{-1/2}$ prediction. The inset presents the empirical scaling of Re_{δ_ν} with respect to k^+ to demonstrate the gradual approach to smooth-wall conditions ($Re_{\delta_\nu} \approx 50$).

value $Re_{\delta_\nu} \approx 50$ has not yet been reached for our present k^+ range. As seen in the inset of figure 14(*d*) however, the $Re_{\delta_\nu} \approx 50$ limit at crests may eventually be attained owing to the continual growth with k^+: $Re_{\delta_\nu} = 3.1(k^+)^{0.46}$. This predicts the smooth-wall limit, $Re_{\delta_\nu} \approx 50$, to be reached once $k^+ \approx 420$ or $k_s^+ = (k_s/k)k^+ \approx (2.7)(420) \approx 1140$. The approach to local smooth-wall conditions at crests may tie to a regime transition at even-higher k^+ beyond the fully rough regime, where the local boundary layers can become turbulent (Kraichnan 1962; Grossmann & Lohse 2011). The behaviour of such a regime, if it exists, would likely have implications in atmospheric flows for instance, where k_s^+ can approach $O(10^5)$ (Kanda *et al.* 2007). Moreover, the existence of this regime will be contingent on extended attached-flow regions existing locally, such that the local boundary layer may develop. These conditions may depend on the strength of the local shear which will generally grow with k^+ and will change depending on the rough surface considered. Consequently, our $k^+ \approx 420$ extrapolation is specific to our present surface and is likely to change when considering alternative surfaces.

An alternative view of the approach towards local smooth-wall conditions at crests can be quantified by measuring the relative difference between the viscous sublayer thickness $\delta^*_{\nu,r}$ and conductive sublayer thickness $\delta^*_{\theta,r}$ at crests compared to smooth walls, $\delta^*_{\nu,s}$, $\delta^*_{\theta,s}$ (the *r* and *s* subscripts denote rough- and smooth-wall values, respectively). These values are reported in figure 15. Here, the data show a tendency towards local smooth-wall

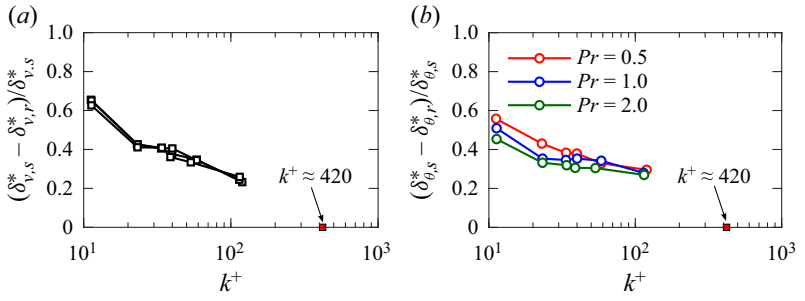

Figure 15. (*a*) Relative difference of the local viscous sublayer thickness measured at the crests, $\delta^*_{v,r} \equiv \delta_{v,r}u_*/\nu$ (the r subscript denotes the value for the rough wall), for $k^+ \geq 11$, compared to the smooth-wall value $\delta^*_{v,s} \approx 7.3$ (the subscript s denotes the smooth-wall value). The extrapolation to $k^+ \approx 420$, where smooth-wall conditions (figure 14*d*, inset) may be expected, is shown as a red square marker. (*b*) Same as (*a*) but for the conductive sublayer thickness, δ^*_θ, at varying Pr. For $Pr = \{0.5, 1.0, 2.0\}$, $\delta^*_{\theta,s} \approx \{9.2, 7.3, 5.8\}$.

conditions with increasing k^+, with our highest $k^+ \approx 111$ attaining approximately 80 % of the smooth-wall value. Our extrapolation from the inset of figure 14(*d*), which predicted the local smooth-wall transition at $k^+ \approx 420$, is also included in figure 15 (red squares). The figure 15 data appear to show a gradual slow-down of the approach to local smooth-wall conditions with increasing k^+. Though our $k^+ \approx 420$ extrapolation for local smooth-wall conditions may perhaps be plausible based on the trends on $\delta^*_{v,r}$ (i.e. the momentum field), this extrapolation is almost certainly not valid for $\delta^*_{\theta,r}$ (i.e. the thermal field), where the slow-down of growth with k^+ is more drastic.

Having provided evidence in the time-averaged flow that heat transfer may be driven locally through a Reynolds-analogy-type behaviour, we now provide an instantaneous view to this behaviour in figure 16, showing joint-p.d.f.s (j.p.d.f.s) between the primitively scaled viscous skin-friction and local heat transfer, $\widehat{C_f}$ and $\widehat{St}$, respectively. We include j.p.d.f.s computed from a smooth-wall DNS (coloured contours), and 'crestward' locations, which sample regions local to the roughness crests, $0.95k \leq z_w \leq k$. Emerging for both transitional $k^+ \approx 33$ (figure 16*a–c*) and fully rough $k^+ \approx 111$ (figure 16*d–f*) is a smooth-wall-like correlation between the local skin-friction and heat transfer at crestward locations running closely parallel to the Reynolds-analogy line $\widehat{C_f}/2 = \widehat{St}Pr^{2/3}$. The crestward j.p.d.f.s for both $k^+ \approx 33$ and $k^+ \approx 111$ tend to show greater standard deviations (width of the j.p.d.f.s) compared to the smooth wall which can be interpreted as a Re_{δ_v} effect. With increasing k^+ (and thereby Re_{δ_v}), the crestward p.d.f.s shrink closer towards the smooth-wall p.d.f. The approach towards the smooth-wall mean values of $\widehat{C_f}$, $\widehat{St}$, square markers shown in figure 14(*a*,*b*), are also included in figure 16.

A useful implication of these local smooth-wall scaling results at the crests is that they enable one to predict the crest skin-friction and heat transfer, relative to, say, the global friction and heat transfer in the form of the globally averaged crest velocity and temperature $U_k \equiv U(z = k)$, $\Theta_k \equiv \Theta(z = k)$. Here, we make use of the scalings we report in figure 17, where the relation to the primitive viscous–conductive quantities, (δ_v, u_{δ_v}), (δ_θ, θ_{δ_θ}), are linked to the globally averaged crest values U_k, Θ_k and k^+. Specifically, figure 17 reformulates the original primitive scaling results presented in figure 14 to now adopt normalisations on the global friction velocity U_τ and globally averaged crest values U_k, Θ_k for use in prediction. Notably in figure 17(*b*), we observe the velocity outside the viscous sublayer follows $u_{\delta_v} \approx 0.75U_k \approx (0.75)(4.7)U_\tau$, i.e. $u_{\delta_v} \propto U_\tau$, as was proposed by Owen & Thomson (1963) and Yaglom & Kader (1974), leading to

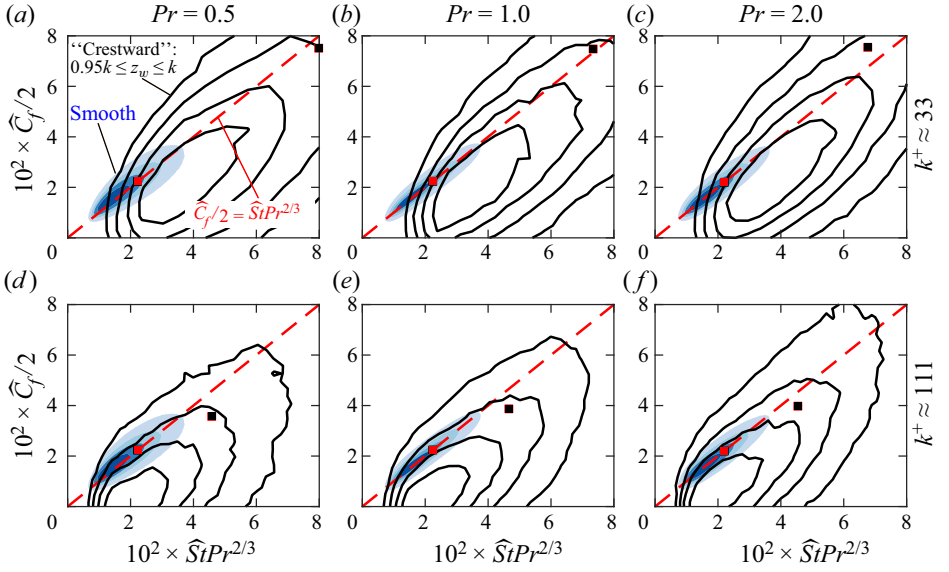

Figure 16. (Black) Conditional joint-p.d.f.s between the local viscous skin-friction coefficient $\widehat{C_f}/2 \equiv \tau_v/(\rho u_{\delta_v}^2)$ and local Stanton number $\widehat{St} \equiv q_w/(\rho c_p u_{\delta_v} \theta_{\delta_\theta})$ for $Pr = 0.5$–2.0 at (*a–c*) $k^+ \approx 33$ and (*d–f*) $k^+ \approx 111$. The rough-wall data are conditionally sampled at regions local to crests: $0.95k \leq z_w \leq k$ and the normalisation choice enables direct comparison to smooth-wall DNS (coloured contours). Each contour level encloses 20–80 % of the total probability in increments of 20 %. The Reynolds-analogy line, $\widehat{C_f}/2 = \widehat{St}Pr^{2/3}$ (dashed red line), forms the principal axes for the smooth walls and appears approximately parallel in crestward regions. The mean values measured at crests (cf. figure 14*a*,*b*) are marked by the black squares and the mean values for the smooth wall DNS are marked by red squares.

the eventual $\delta_\nu^+ \sim (k^+)^{1/2}$ prediction in (2.8*a*,*b*), a scaling that is affirmed by our data in figure 17(*a*) for $k^+ \gtrsim 33$. A likewise proportionality is observed at the conductive sublayer for heat transfer: $\theta_{\delta_\theta} \approx 0.75\Theta_k$. We now demonstrate how these results can be used for a local skin-friction and heat transfer prediction. Recognising that in the linear viscous–conductive regions, the velocity and temperature gradients are constant up to δ_ν and δ_θ, respectively (cf. figure 13*a*,*b*), we set $\tau_v/\rho = \nu u_{\delta_v}/\delta_\nu$ and $q_w/(\rho c_p) = \alpha\theta_{\delta_\theta}/\delta_\theta$. These relations may then be inserted into a local skin-friction coefficient for crests, $C_{f,\mathrm{crest}}$, and for a Stanton number, St_{crest}:

$$\frac{C_{f,\mathrm{crest}}}{2} \equiv \frac{\tau_v}{\rho U_k^2} = \frac{\nu u_{\delta_v}/\delta_\nu}{U_k^2} = \left(\frac{u_{\delta_v}}{U_k}\right)\left(\frac{1}{U_k^+}\right)\left(\frac{1}{\delta_\nu^+}\right)$$
$$\approx (0.75)\left(\frac{1}{4.7}\right)\left(\frac{1}{0.7}\right)(k^+)^{-0.50} \approx 0.23(k^+)^{-0.50}, \tag{4.3}$$

$$St_{\mathrm{crest}} \equiv \frac{q_w/(\rho c_p)}{U_k\Theta_k} = \frac{\alpha\theta_{\delta_\theta}/\delta_\theta}{U_k\Theta_k} = Pr^{-1}\left(\frac{\theta_{\delta_\theta}}{\Theta_k}\right)\left(\frac{1}{U_k^+}\right)\left(\frac{1}{\delta_\theta^+}\right)$$
$$\approx (0.75)\left(\frac{1}{4.7}\right)\left(\frac{1}{0.97}\right)(k^+)^{-0.42}Pr^{-0.72} \approx 0.16(k^+)^{-0.42}Pr^{-0.72}, \tag{4.4}$$

where we have made use of the various results of figure 17 for the numerical prefactors. The relations (4.3)–(4.4) thus allow one to determine the viscous–conductive fluxes at the crests provided only k^+ and Pr within a constant of proportionality. These results then

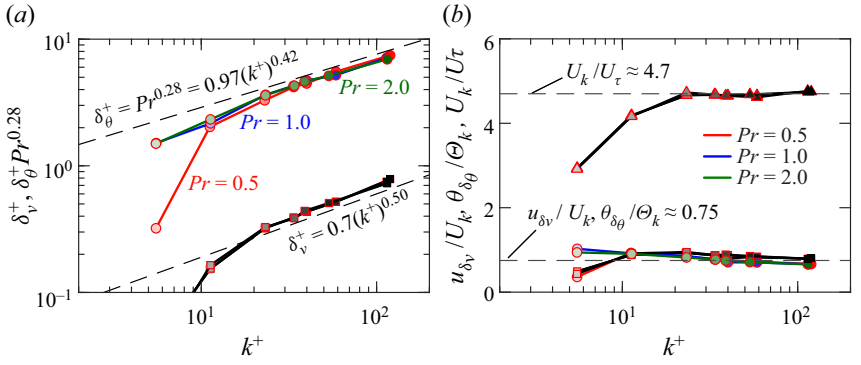

Figure 17. (*a*) Scaling behaviours of δ_θ^+ and δ_v^+ at the crests, with empirical fits provided. For clarity, δ_v^+ has been staggered down by a decade. (*b*) Various scaling behaviours of local viscous–conductive quantities at the crest linked to the globally averaged crest velocity and temperature, U_k, Θ_k.

demonstrate how a $p = 1/2$ type scaling in heat transfer, $St_{crest} \sim (k^+)^{-p}$ as originally put forward in the Prandtl–Blasius ideas of Owen & Thomson (1963) and Yaglom & Kader (1974) can be favoured for prediction. The key distinction here being to consider the heat transfer only in regions where the flow is attached and exposed to high-shear, where presently, we have demonstrated this case for roughness crests. Much like the original $p = 1/2$ theories, these predictions are to be restricted to the high-k^+ or fully rough regime, $k^+ \gtrsim 33$, where the various scalings in (4.3)–(4.4) remain valid. Finally, it is worth mentioning that one may expect the validity of this local Prandtl–Blasius scaling to be restricted to regions of mild curvature, such that the local flow remains attached. For our present 3-D sinusoids, this curvature is characterised by the wavelength-to-height ratio $\lambda/k = 7.1$. Overall, this paper suggests that the ratio of attached to separated flow regions is key to modelling the effect of roughness topography on heat-transfer (and drag) behaviour.

4.4. *Local roughness trough behaviour*

Having seen at roughness crests that we may observe a Reynolds-analogy-like behaviour, we now provide an opposite view to this at roughness trough regions. Unlike crests, the flow in the vicinity of troughs is predominantly driven by a low-shear, reversed flow (cf. figure 8), such that we may expect vastly different behaviours to those we observed in § 4.3 at crests. Figure 18(*a*,*b*) demonstrates this with time-averaged velocity and temperature profiles ($Pr = 1.0$) at trough regions. Here, the profiles are scaled on the crest values, U_k, Θ_k and roughness height k, as opposed to the local friction velocity u_* as with figure 13, since troughs are low-shear regions with $u_* \to 0$. The disparate behaviour between velocity and temperature is apparent: the near-wall flow is reversed ($u_{trough} < 0$) with distinct minima in the velocity emerging, a feature entirely absent in the temperature profiles. The reversed flow is predominantly confined to $z_{trough}/k \lesssim 1$, and may perhaps serve as the primary flow which drives heat transfer locally. The insets of figure 18(*a*,*b*) show the profiles rescaled by viscous–conductive quantities situated through the local second derivative extrema, identical to the method adopted for crests in figure 13(*a*,*b*). Although these normalisations appear adequate for collapsing the temperature profiles, this is not the case for the streamwise velocity, perhaps indicating the existence of some other velocity and length scale as being appropriate. The absence of any Reynolds-analogy-type scaling at troughs may be further illustrated by the results of figure 18(*c*,*d*), where

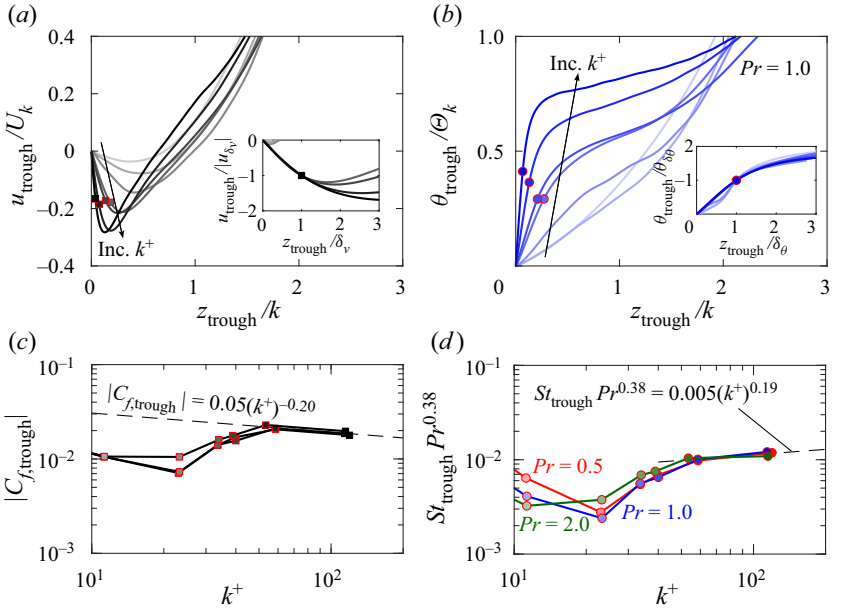

Figure 18. (*a*) Time- and phase-averaged profiles at roughness troughs. Here, z_{trough} measures the wall-normal distance taking roughness troughs (cf. figure 6*b*) as the origin. The local viscous sublayer and the velocity at this location, δ_ν, u_{δ_ν} (square markers), is situated by maxima of the second derivative $\mathrm{d}^2u_{\mathrm{trough}}/\mathrm{d}z^2$. The inset rescales the profiles on δ_ν, u_{δ_ν}. (*b*) Same as (*a*) but for temperature at $Pr = 1.0$. (*c*,*d*) Local skin-friction coefficient and Stanton number at the troughs, normalised on the global crest velocity and temperature, $|C_{f,\mathrm{trough}}|/2 \equiv |\tau_\nu|/(\rho U_k^2)$, $St_{\mathrm{trough}} \equiv q_w/(\rho c_p U_k \Theta_k)$, with empirical fits provided. The absolute value of skin-friction is taken to enable plotting on log-axes.

we show the locally measured skin-friction coefficient, $C_{f,\mathrm{trough}}/2 \equiv \tau_\nu/(\rho U_k^2)$, and Stanton number, $St_{\mathrm{trough}} \equiv q_w/(\rho c_p U_k \Theta_k)$. These normalisation choices are identical to those chosen in (4.3)–(4.4) for crests to contrast with the Reynolds-analogy-like scaling behaviour that was seen at crests, $C_{f,\mathrm{crest}} \sim (k^+)^{-0.50}$, $St_{\mathrm{crest}}Pr^{0.72} \sim (k^+)^{-0.42}$. At trough regions, we instead find $|C_{f,\mathrm{trough}}| \sim (k^+)^{-0.20}$, $St_{\mathrm{trough}}Pr^{0.38} \sim (k^+)^{0.19}$, following neither the $St_{\mathrm{trough}}Pr^{1/2} \sim (k^+)^{-1/4}$ to be expected from surface renewal or the $St_{\mathrm{trough}}Pr^{2/3} \sim (k^+)^{-1/2}$ of Prandtl–Blasius. A contrast in behaviour between crests and troughs may be further visualised by the conditional j.p.d.f.s in figure 19 between the primitively scaled skin-friction coefficient and Stanton number, $\widehat{C_f}$, $\widehat{St}$, respectively. Here, 'troughward' regions, which sample regions local to troughs ($-k \leq z_w \leq -0.95k$) show a vastly different behaviour to the Reynolds-analogy-like behaviour we had proposed for crestward regions originally in figure 16. Notably, the troughward j.p.d.f.s tend to be much wider than the crestward counterparts, indicating a greater prominence of skin-friction and heat-transfer fluctuations in the vicinity of troughs. The formation of a principal axes between $\widehat{C_f}$ and $\widehat{St}$ is perhaps weakly present in the troughward j.p.d.f.s. Moreover, these principal axes do not appear to strongly follow a reversed-flow Reynolds-analogy correlation $-\widehat{C_f}/2 = \widehat{St}Pr^{2/3}$ (dashed red line). Our intention in showcasing these contrasting results at troughs is to highlight the potential for multiple mechanisms to be at play in driving heat transfer locally. Much like at roughness crests where our analysis showed that a pure Reynolds-analogy-driven heat transfer did not quite emerge, it is possible that roughness troughs may experience the same crossover among multiple mechanisms. Unravelling the heat transfer mechanisms which underpin

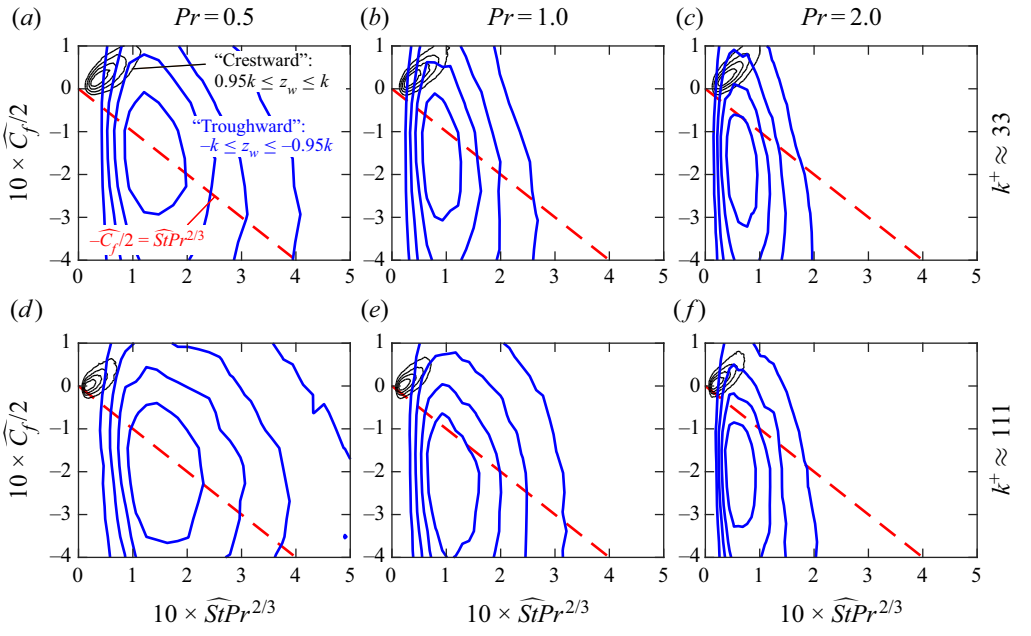

Figure 19. Conditional j.p.d.f.s between the primitive local skin-friction coefficient $\widehat{C_f}/2 \equiv \tau_v/(\rho u_{\delta_v}^2)$ and local Stanton number $\widehat{St} \equiv q_w/(\rho c_p |u_{\delta_v}| \theta_{\delta_\theta})$ (the absolute value of u_{δ_v} is taken to circumvent negative values for St) at varying Pr and for (*a–c*) $k^+ \approx 33$; (*d–f*) $k^+ \approx 111$. The blue lines sample regions local to roughness troughs: $-k \leq z_w \leq -0.95k$ and is contrasted with the crestward j.p.d.f.s originally shown in figure 16 (black lines). A reversed-flow Reynolds-analogy line, $-\widehat{C_f}/2 = \widehat{St} Pr^{2/3}$ is given by the dashed red line.

these flow-separated trough regions will require a deeper investigation, but is outside the scope of our present work.

5. Full-scale heat transfer predictions

Having seen the success of the Kolmogorov–Brutsaert fully rough model for the mean heat transfer (§ 4.2), we will examine here the implications this has on full-scale heat transfer predictions. One of the primary quantities of interest in heat transfer prediction is the Nusselt number, $Nu \equiv ReStPr$ (Kays & Crawford 1993), defined on an outer-scale Reynolds number, $Re \equiv hU_h/\nu$, and an outer-scale Stanton number, $St \equiv 1/(U_h^+ \Theta_h^+) \equiv (C_F/2)^{1/2}/\Theta_h^+$, where $C_F \equiv 2/(U_h^{+2})$ is a global friction coefficient encompassing both pressure and viscous drag. These use the velocity and temperature evaluated at the channel centreline: $U_h \equiv U(z = h)$, $\Theta_h \equiv \Theta(z = h)$.

Recall that in minimal channels, the mean profiles above the critical height z_c is unphysical and will need to be modelled before we evaluate U_h and Θ_h. Presently, we have computed U_h and Θ_h from our DNS cases by extending the logarithmic regions towards the channel centreline, replacing the unphysical data beyond z_c. Doing so, we also neglect wake contributions to the mean profile. For additional comparison, we will adopt models which employ the logarithmic profiles (1.1) and (1.2) evaluated at $z = h$, again neglecting wake contributions to obtain U_h^+ and Θ_h^+, respectively. The results can then be combined to obtain (cf. Kays & Crawford 1993, (13)–(48))

$$NuRe^{-1}Pr^{-1} \equiv St = \frac{C_F/2}{(\kappa/\kappa_\theta) + \sqrt{C_F/2}/St_k}. \tag{5.1}$$

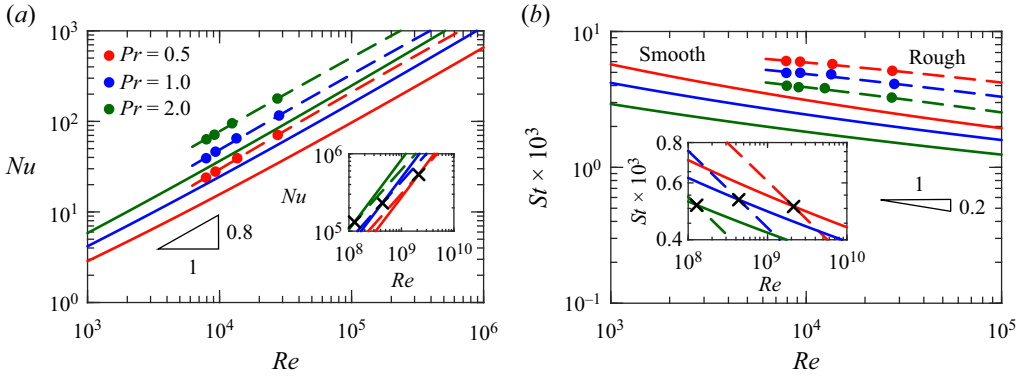

Figure 20. (*a*) Nusselt number and (*b*) Stanton number dependence on the Reynolds number. Circle markers are from rough wall DNS at $k/h = 1/18$. The solid lines are model lines obtained using the smooth-wall log law, whilst the dashed lines are from the fully rough models. The insets highlight the crossover points (crosses) between smooth- and rough-wall curves at high Re.

For model parameters, we use $\kappa \approx 0.4$, $\kappa_\theta \approx 0.46$, that we have used throughout our manuscript. We use the fully rough model $\Delta U^+ = (1/\kappa)\log(2.7k^+) - 3.5$ (cf. figure 7*c*) and the fully rough model of Brutsaert (1975*b*): $St_k^{-1} = 6.5(z_0^+)^{1/4}Pr^{1/2} - 4.6$ (figure 11*b*).

Shown in figure 20 are the variations of Nu and St for our present study using $k/h = 1/18$. The adopted model (dashed lines) agrees well with our present DNS (markers) and for intermediate $Re \approx 10^4$–10^6, roughly follow the well-known smooth-wall scaling $Nu \sim Re^{0.8}$, $St \sim Re^{-0.2}$ (Kays & Crawford 1993). The smooth wall curves of figure 20 (solid lines), included for comparison, are obtained by adopting the same equation (5.1) as with the rough walls but with $\Delta U^+ = 0$ and $\Delta\Theta^+ = 0$ when obtaining U_h^+, Θ_h^+ from the log-equations (1.1*a*) and (1.2*a*). In the insets of figure 20, we illustrate the paradox introduced in figure 7(*b*,*d*) concerning the effects of heat transfer augmentation at high Reynolds number when extrapolating the rough-wall log-intercepts (4.1*a*)–(4.1*c*) towards $Re \to \infty$, $k^+ \to \infty$. Whilst for intermediate Re, both Nu and St are larger for rough walls, indicating a heat transfer augmentation. There is an eventual crossover point with the smooth-wall curves. In the limit of large Re, we see that the fully rough model no longer predicts augmented heat transfer relative to a smooth wall, standing in contrast to how rough-wall heat transfer is conventionally viewed (Dipprey & Sabersky 1963; Owen & Thomson 1963; Bons *et al.* 2001). Despite the largely successful predictive capabilities of Brutsaert's model having been established for the present k^+ range in our study, a more concrete conclusion concerning the true asymptotic form of heat transfer as $k^+ \to \infty$, $Re \to \infty$ remains unsettled. It is worth highlighting that the data shown in figure 20 are for a fixed $h/k = 18$. In practice, this may not always be the case, such as in river beds with $h/k = O(1)$ (Rouzes *et al.* 2019). Such flows may have poorly defined logarithmic regions (Jiménez 2004) which would make our model curves of figure 20 inapplicable. Provided h/k is not too small and Re is sufficiently large however, such flows will maintain a better-defined logarithmic region and we would expect the same trends we show in figure 20 to hold. Noteworthy is that several DNS studies (e.g. Chan *et al.* 2015; Thakkar *et al.* 2018; Ma *et al.* 2020) have found that despite using $h/k = O(1)$, the log-intercept measurements can still remain robust.

6. Conclusion

We have investigated the phenomenology surrounding rough-wall heat transfer by scrutinising a comprehensive DNS dataset, systematically varying both the Prandtl number, Pr, and roughness Reynolds number, k^+. Our work begins to address the uncertainty that lingers concerning the asymptotic form of heat transfer in the fully rough regime by testing many of the hypothesised phenomenologies proposed to describe this regime (Li *et al.* 2017, 2020). Although it appears that bulk measures from our data affirm the surface-renewal phenomenology (Brutsaert 1975*b*) consistent with Kays & Crawford (1993), which proposes the interfacial temperature scaling $\Theta_i^+ \sim (k^+)^p Pr^m$ with $p = 1/4$, $m = 1/2$ in the fully rough regime, the mechanism locally is more complex. Nevertheless, an energy-cascade-type scaling for ensemble-averaged measures of the dissipation, $\varepsilon \sim U_\tau^3/k$, a crucial element to the surface renewal theory, is upheld even in the vicinity of the roughness elements. We show that the ideas underpinning the $p = 1/2$ Prandtl–Blasius, Reynolds-analogy-type scaling can remain robust in certain regions where the flow remains attached and is exposed to high shear such as roughness crests. This manifests as an empirical local heat transfer scaling, $St_{crest} Pr^{0.72} \sim (k^+)^{-0.42}$, lying close to the $St_{crest} Pr^{2/3} \sim (k^+)^{-1/2}$ to be expected from Reynolds analogy. However, the Reynolds-analogy scaling is violated in regions locally exposed to reversed flow and weak shear. The mechanisms which drive rough-wall heat transfer then are not captured by any singular mechanism, but likely an ensemble of different behaviours locally.

While the model of Brutsaert (1975*b*) appears largely successful in predicting the mean heat transfer for the k^+-range considered in our present study, the $\Theta_i^+ \sim (k^+)^{1/4}$ predicted by this theory implies a continual decrease in $\Delta\Theta^+$ with k^+, eventually resulting in a negative $\Delta\Theta^+$. That is, roughness may cause a reduction in heat transfer relative to a smooth wall, which stands in contrast to how rough-wall heat transfer is conventionally viewed (e.g. Bons *et al.* 2001) and poses a question concerning the true asymptotic form of rough-wall heat transfer as $k^+ \to \infty$. Examination of the local flow behaviour at crest regions exposed to higher shear shows a continual growth of the local viscous Reynolds number towards the smooth-wall value $Re_{\delta_\nu} \approx 50$, which is potentially indicative of a local smooth-wall-like regime transition. Though higher-k_s^+ data are ultimately needed to affirm the existence of this regime transition (cf. figure 15), we speculate its onset to occur at $k_s^+ \approx 1140$, lying well within the expected range of natural flows (Kanda *et al.* 2007).

Acknowledgements. We are indebted to Professor D. Lohse for having provided helpful feedback in the preparation of this manuscript.

Funding. The authors gratefully acknowledge the support of the Australian Research Council Discovery Project DP200100969. This research was undertaken with the assistance of resources from the National Computational Infrastructure (NCI Australia), an NCRIS enabled capability supported by the Australian Government. The authors also acknowledge the support of additional resources provided by the Pawsey Supercomputing Centre with funding from the Australian Government and the Government of Western Australia. This research was supported by the sustaining and strengthening merit-based access to National Computational Infrastructure (NCI) LIEF Grant (LE190100021) and facilitated by The University of Melbourne.

Declaration of interests. The authors report no conflict of interest.

Author ORCIDs.
Kevin Zhong https://orcid.org/0000-0002-2484-4115;
Nicholas Hutchins https://orcid.org/0000-0003-1599-002X;
Daniel Chung https://orcid.org/0000-0003-3732-364X.

https://doi.org/10.1017/jfm.2023.125 Published online by Cambridge University Press

Re_τ	Pr	$\frac{h}{k}$	k^+	L_x^+	L_y^+	N_x	N_y	N_z	Δx^+	Δy^+	Δz_b^+	Δz_t^+	$\frac{\lambda}{\Delta x}$	$\frac{\lambda}{\Delta y}$	$\frac{k}{\Delta z_b}$	Δt^+	T_s	ΔU^+	$\Delta \Theta^+$
Full-span channel																			
395	0.5	—	—	2493	1246	256	256	300	9.74	4.87	0.34	5.7	—	—	—	0.16	34	—	—
395	1.0	—	—	2493	1246	256	256	300	9.74	4.87	0.34	5.7	—	—	—	0.16	32	—	—
395	2.0	—	—	2493	1246	384	384	440	6.49	3.25	0.20	4.05	—	—	—	0.10	16	—	—
395	0.5	18	22	2493	1246	384	384	620	6.49	3.25	0.28	6.64	24	48	77	0.05	5.4	6.8	2.3
395	1.0	18	22	2493	1246	384	384	620	6.49	3.25	0.28	6.64	24	48	77	0.06	6.4	6.8	4.7
395	2.0	18	22	2493	1246	512	512	820	4.87	2.43	0.24	4.01	32	64	90	0.04	7.1	6.8	9.1
Minimal channel																			
395	0.5	—	—	1091	312	128	64	300	8.52	4.87	0.39	5.46	—	—	—	0.24	445	—	—
395	1.0	—	—	1091	312	128	64	300	8.52	4.87	0.39	5.46	—	—	—	0.24	351	—	—
395	2.0	—	—	1091	312	192	96	384	5.68	3.25	0.30	4.27	—	—	—	0.17	417	—	—
395	0.5	18	22	1091	312	192	64	660	5.68	4.87	0.28	5.54	27	32	77	0.07	181	6.9	2.2
395	1.0	18	22	1091	312	192	64	660	5.68	4.87	0.28	5.54	27	32	77	0.07	150	7.0	4.9
395	2.0	18	22	1091	312	256	128	840	4.26	2.43	0.24	3.76	37	64	90	0.06	62	7.0	9.1

Table 2. Simulation parameters for full-span and minimal channel comparisons. Parameter definitions are the same as in table 1. Note that for full-span channels, $T_s = TU_\tau/h$.

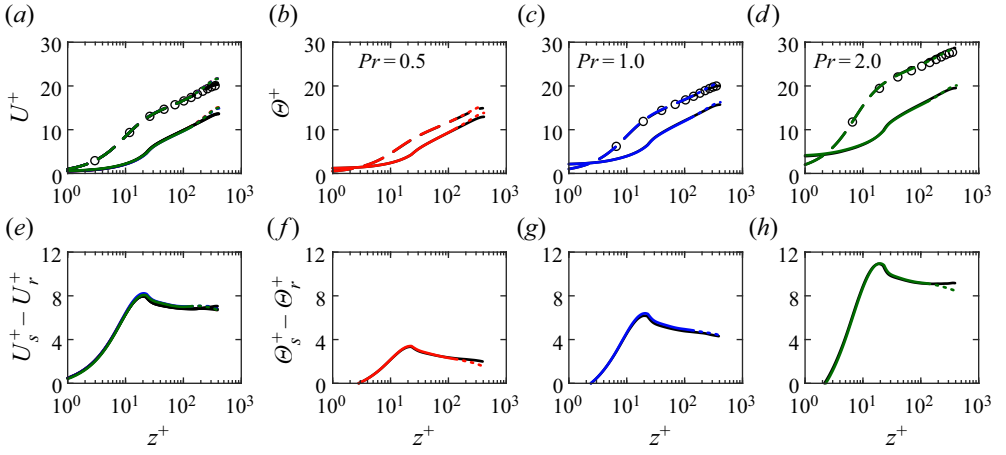

Figure 21. (*a–d*) Mean velocity and temperature profiles comparing full-span (black) to minimal channels (coloured) at $k^+ \approx 22$. Dashed lines correspond to smooth walls while solid lines are for rough walls. The dotted lines demarcate the unphysical region, $z > z_c$. The markers in (*a*) are the data from Moser, Kim & Mansour (1999), while the markers in (*c*,*d*) are from Kozuka, Seki & Kawamura (2009). (*e–h*) Differences of smooth- and rough-wall velocities and temperatures from which ΔU^+, $\Delta\Theta^+$ are computed at $z = z_c$.

Appendix A. Minimal channel influences on heat transfer

In this appendix, we present results comparing full-span and minimal channels at $k^+ \approx 22$, assessing the domain size influences on heat transfer at $Pr = 0.5$, 1.0 and 2.0. The simulations are summarised in table 2. Here, L_x and L_y for smooth- and rough-wall simulations are matched exactly so domain size effects will not influence the results in our comparison. We summarise in figure 21 mean profiles and the difference between smooth- and rough-wall profiles from which ΔU^+ and $\Delta\Theta^+$ are computed at $z = z_c$. Roughness functions quoted in table 2 are within ± 0.2 for ΔU^+ and $\Delta\Theta^+$, which are similar to statistical uncertainties in other minimal channel studies (MacDonald *et al.* 2017, 2019; Endrikat *et al.* 2021). Given the good agreement between the full-span and minimal channels across the Pr values with which we are concerned, we conclude that the use of minimal channels will be adequate in our study of the near-wall effects of rough-wall heat transfer.

Appendix B. Low-Reynolds-number effects on heat transfer

A well-documented result in wall-bounded turbulence is that a low Re_τ can alter the mean momentum and temperature balance of the flow (Wei 2018). This can shift the logarithmic region, affecting the measurement of ΔU^+ and $\Delta\Theta^+$ (Chan *et al.* 2015; Pirozzoli *et al.* 2016; Alcántara-Ávila *et al.* 2018; Thakkar *et al.* 2018; MacDonald *et al.* 2019). This low-Re_τ influence on heat transfer was investigated by MacDonald *et al.* (2019) at $Pr = 0.7$, $k^+ \approx 22$ for $Re_\tau \approx 395$ and 590, who found that the differences were primarily in the outer region of the flow such that $Re_\tau \approx 395$ would be adequate for studying near-wall effects. The purpose of this appendix will be to affirm this result for $Pr = 0.5$, 1.0, 2.0 with the simulations in table 3. The mean velocity and temperature profiles presented in figure 22(*a–d*) show that $Re_\tau \approx 395$ is satisfactory for capturing much of the near-wall behaviour across all Pr. The main discrepancies emerge at the outer-edge of the log layer in the vicinity of $z = z_c$. This is carried forward into the

https://doi.org/10.1017/jfm.2023.125 Published online by Cambridge University Press

Re_τ	Pr	$\frac{h}{k}$	k^+	L_x^+	L_y^+	N_x	N_y	N_z	Δx^+	Δy^+	Δz_b^+	Δz_t^+	$\frac{\lambda}{\Delta x}$	$\frac{\lambda}{\Delta y}$	$\frac{k}{\Delta z_b}$	Δt^+	T_s	ΔU^+	$\Delta\Theta^+$
395	0.5	—	—	1091	312	128	64	300	8.52	4.87	0.39	5.46	—	—	—	0.24	445	—	—
395	1.0	—	—	1091	312	128	64	300	8.52	4.87	0.39	5.46	—	—	—	0.24	351	—	—
395	2.0	—	—	1091	312	192	96	192	5.68	3.25	0.30	4.27	—	—	—	0.17	417	—	—
395	0.5	18	22	1091	312	192	64	660	5.68	4.87	0.28	5.54	27	32	79	0.07	181	6.9	2.2
395	1.0	18	22	1091	312	192	64	660	5.68	4.87	0.28	5.54	27	32	79	0.07	150	7.0	4.9
395	2.0	18	22	1091	312	256	128	840	4.26	2.43	0.24	3.76	37	64	92	0.06	62	7.0	9.1
590	0.5	—	—	1086	310	128	64	440	8.48	4.85	0.40	5.56	—	—	—	0.20	93	—	—
590	1.0	—	—	1086	310	128	64	440	8.48	4.85	0.40	5.56	—	—	—	0.19	91	—	—
590	2.0	—	—	1086	310	192	96	600	5.66	3.23	0.21	4.43	—	—	—		175	—	—
590	0.5	27	22	1086	310	192	64	820	5.66	4.85	0.28	5.50	27	32	79	0.07	135	7.0	2.5
590	1.0	27	22	1086	310	192	64	820	5.66	4.85	0.28	5.50	27	32	79	0.07	137	6.8	4.7
590	2.0	27	22	1086	310	256	128	1060	4.24	2.42	0.24	3.76	37	64	92	0.06	149	6.8	8.9

Table 3. Simulation parameters for studying Re_τ influences at a fixed $k^+ \approx 22$. Refer to table 1 for definitions of table entries.

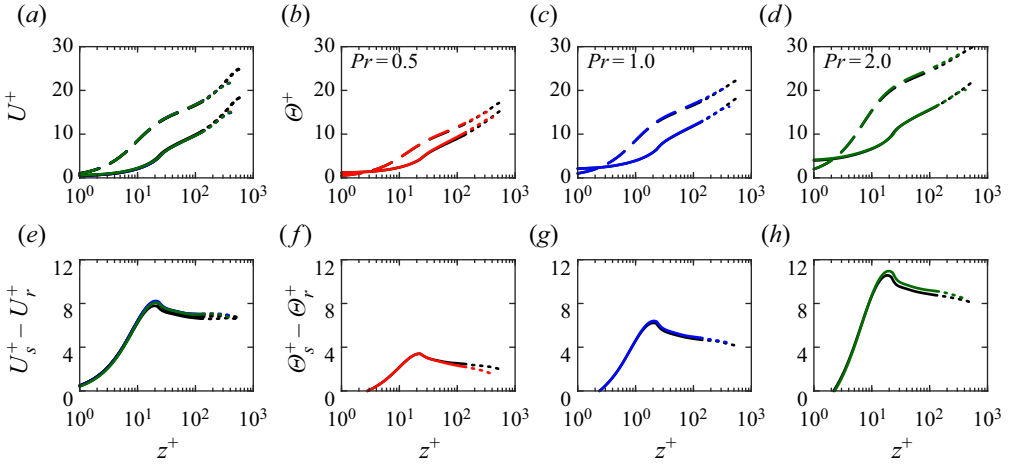

Figure 22. (*a–d*) Mean velocity and temperature profiles at matched $k^+ \approx 22$ for $Re_\tau \approx 590$ (black) and $Re_\tau \approx 395$ (coloured). Dashed lines correspond to smooth walls while solid lines are for rough walls. The dotted lines demarcate the unphysical region, $z > z_c$. (*e–h*) Differences of smooth- and rough-wall velocities and temperatures from which ΔU^+, $\Delta\Theta^+$ are computed at $z = z_c$.

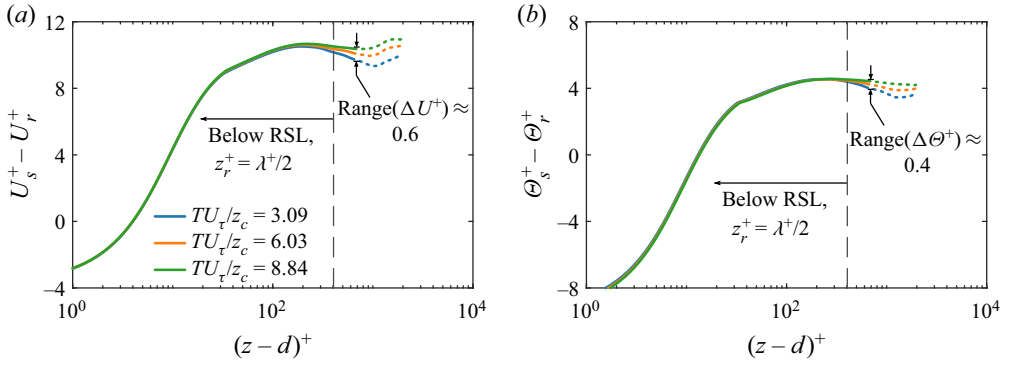

Figure 23. The difference profiles between (*a*) streamwise velocity and (*b*) temperature for $k^+ = 111$ and $Pr = 1.0$ obtained from progressively longer time-averaging periods TU_τ/z_c. The log-intercepts, ΔU^+ and $\Delta\Theta^+$, are computed as the difference profiles at the minimal channel critical heights (demarcated by the dotted lines), $z_c^+ = 0.4L_y^+$. The roughness sublayer (RSL) height is demarcated by the dashed vertical line, $z_r^+ = \lambda^+/2$ (Chan *et al.* 2018).

differences of smooth- and rough-wall velocities and temperatures (figure 22*e–h*), where ΔU^+ and $\Delta\Theta^+$ are found to vary by ± 0.3. These variations are similar to the statistical uncertainties we present in our main results of § 3.2. In light of this finding and the fact that the roughness sublayer region $z_r^+ \approx \lambda^+/2 \approx 80$ (Chan *et al.* 2018) is still adequately captured by $Re_\tau \approx 395$, we deem $Re_\tau \approx 395$ as a suitable lower-bound for our parameter space.

Appendix C. Statistical sampling uncertainties in $k^+ = 111$ cases

Here, we provide details on the characteristic statistical uncertainties for our $k^+ \approx 111$ cases in table 1, which have time-averaging periods $TU_\tau/z_c \approx 8.8$–13.6. Shown in figure 23 are the difference profiles between smooth and rough walls for the mean

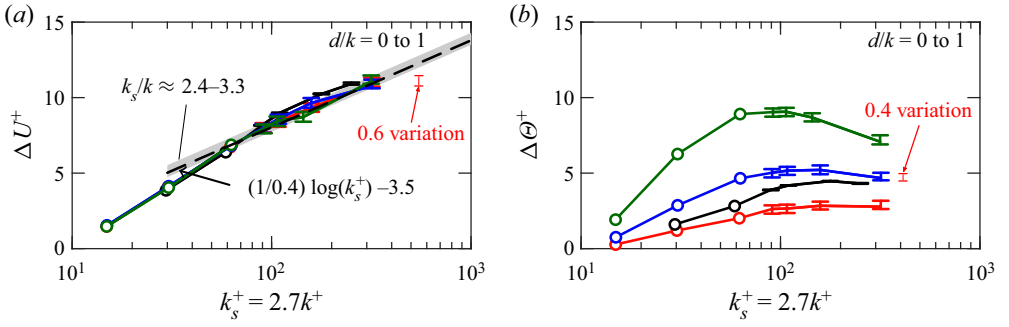

Figure 24. Reproduced figure 7(*c*,*d*) showing roughness functions (*a*) ΔU^+ and (*b*) $\Delta\Theta^+$. We highlight (in red) the range $(\Delta U^+) \approx 0.6$, range $(\Delta\Theta^+) \approx 0.4$ scatter that was presented in figure 23.

velocity and temperature, for $k^+ = 111$, $Pr = 1.0$ at progressively longer time-averaging periods. The near-wall, roughness sublayer region, $(z-d)^+ < z_r^+$, remains well-captured among all time-averaging periods. The log-intercepts, ΔU^+ and $\Delta\Theta^+$, are taken to be the values at the minimal channel critical height $(z-d)^+ = z_c^+$, which show scatters of approximately 0.4 and 0.6 for ΔU^+ and $\Delta\Theta^+$, respectively. These scatters are contextualised in figure 24 (a reproduced figure 7*c*,*d* of our present work) by overlaying these error bands of 0.6 and 0.4 for ΔU^+ and $\Delta\Theta^+$, respectively. Here, we observe that these errors are commensurate to the uncertainties caused by the $d/k \in [0, 1]$ variations investigated in § 3.2 and likewise, do not significantly alter the trends we observe in the fully rough regime.

References

Abderrahaman-Elena, N., Fairhall, C.T. & García-Mayoral, R. 2019 Modulation of near-wall turbulence in the transitionally rough regime. *J. Fluid Mech.* **865**, 1042–1071.

Abe, H. & Antonia, R.A. 2019 Mean temperature calculations in a turbulent channel flow for air and mercury. *Intl J. Heat Mass Transfer* **132**, 1152–1165.

Alcántara-Ávila, F., Hoyas, S. & Pérez-Quiles, M.J. 2018 DNS of thermal channel flow up to $Re_\tau = 2000$ for medium to low Prandtl numbers. *Intl J. Heat Mass Transfer* **127**, 349–361.

Alcántara-Ávila, F., Hoyas, S. & Pérez-Quiles, M.J. 2021 Direct numerical simulation of thermal channel flow for $Re_\tau = 5000$ and $Pr = 0.71$. *J. Fluid Mech.* **916**, A29.

Anderson, W. 2013 Passive scalar roughness lengths for atmospheric boundary layer flow over complex, fractal topographies. *Environ. Fluid Mech.* **13** (5), 479–501.

Bird, R.B., Stewart, W.E. & Lightfoot, E.N. 2007 *Transport Phenomena*, 2nd edn. Wiley.

Bons, J.P., Taylor, R.P., Mcclain, S.T. & Rivir, R.B. 2001 The many faces of turbine surface roughness. *Trans. ASME J. Turbomach.* **123** (4), 739–748.

Brutsaert, W. 1975*a* The roughness length for water vapor, sensible heat, and other scalars. *J. Atmos. Sci.* **32** (10), 2028–2031.

Brutsaert, W. 1975*b* A theory for local evaporation (or heat transfer) from rough and smooth surfaces at ground level. *Water Resour. Res.* **11** (4), 543–550.

Brutsaert, W. 1982 *Evaporation into the Atmosphere: Theory, History and Applications*, vol. 1. Springer Science & Business Media.

Chan, L., MacDonald, M., Chung, D., Hutchins, N. & Ooi, A. 2015 A systematic investigation of roughness height and wavelength in turbulent pipe flow in the transitionally rough regime. *J. Fluid Mech.* **771**, 743–777.

Chan, L., MacDonald, M., Chung, D., Hutchins, N. & Ooi, A. 2018 Secondary motion in turbulent pipe flow with three-dimensional roughness. *J. Fluid Mech.* **854**, 5–33.

Chan-Braun, C., García-Villalba, M. & Uhlmann, M. 2011 Force and torque acting on particles in a transitionally rough open-channel flow. *J. Fluid Mech.* **684**, 441–474.

CHENG, H. & CASTRO, I.P. 2002 Near wall flow over urban-like roughness. *Boundary-Layer Meteorol.* **104** (2), 229–259.

CHUNG, D., CHAN, L., MACDONALD, M., HUTCHINS, N. & OOI, A. 2015 A fast direct numerical simulation method for characterising hydraulic roughness. *J. Fluid Mech.* **773**, 418–431.

CHUNG, D., HUTCHINS, N., SCHULTZ, M.P. & FLACK, K.A. 2021 Predicting the drag of rough surfaces. *Annu. Rev. Fluid Mech.* **53**, 439–471.

CLAUSER, F.H. 1954 Turbulent boundary layers in adverse pressure gradients. *J. Aero. Sci.* **21** (2), 91–108.

COCEAL, O., DOBRE, A., THOMAS, T.G. & BELCHER, S.E. 2007 Structure of turbulent flow over regular arrays of cubical roughness. *J. Fluid Mech.* **589**, 375–409.

DANCKWERTS, P.V. 1951 Significance of liquid-film coefficients in gas absorption. *Ind. Engng Chem.* **43** (6), 1460–1467.

DAWSON, D.A. & TRASS, O. 1972 Mass transfer at rough surfaces. *Intl J. Heat Mass Transfer* **15** (7), 1317–1336.

DIMOTAKIS, P.E. 2000 The mixing transition in turbulent flows. *J. Fluid Mech.* **409**, 69–98.

DIMOTAKIS, P.E. 2005 Turbulent mixing. *Annu. Rev. Fluid Mech.* **37**, 329–356.

DIPPREY, D.F. & SABERSKY, R.H. 1963 Heat and momentum transfer in smooth and rough tubes at various Prandtl numbers. *Intl J. Heat Mass Transfer* **6** (5), 329–353.

DONZIS, D.A. & SREENIVASAN, K.R. 2010 The bottleneck effect and the Kolmogorov constant in isotropic turbulence. *J. Fluid Mech.* **657**, 171.

DOOSTTALAB, A., ARAYA, G., NEWMAN, J., ADRIAN, R.J., JANSEN, K. & CASTILLO, L. 2016 Effect of small roughness elements on thermal statistics of a turbulent boundary layer at moderate Reynolds number. *J. Fluid Mech.* **787**, 84.

DURBIN, P.A. & PETTERSSON-REIF, B.A. 2011 *Statistical Theory and Modeling for Turbulent Flows*. Wiley.

ENDRIKAT, S., MODESTI, D., GARCÍA-MAYORAL, R., HUTCHINS, N. & CHUNG, D. 2021 Influence of Riblet shapes on the occurrence of Kelvin–Helmholtz rollers. *J. Fluid Mech.* **913**, A37.

FADLUN, E.A., VERZICCO, R., ORLANDI, P. & MOHD-YUSOF, J. 2000 Combined immersed-boundary finite-difference methods for three-dimensional complex flow simulations. *J. Comput. Phys.* **161** (1), 35–60.

FAIRHALL, C.T., ABDERRAHAMAN-ELENA, N. & GARCÍA-MAYORAL, R. 2019 The effect of slip and surface texture on turbulence over superhydrophobic surfaces. *J. Fluid Mech.* **861**, 88–118.

FLACK, K.A. & SCHULTZ, M.P. 2010 Review of hydraulic roughness scales in the fully rough regime. *Trans. ASME J. Fluids Engng* **132** (4), 041203.

FOROOGHI, P., STRIPF, M. & FROHNAPFEL, B. 2018*a* A systematic study of turbulent heat transfer over rough walls. *Intl J. Heat Mass Transfer* **127**, 1157–1168.

FOROOGHI, P., WEIDENLENER, A., MAGAGNATO, F., BÖHM, B., KUBACH, H., KOCH, T. & FROHNAPFEL, B. 2018*b* DNS of momentum and heat transfer over rough surfaces based on realistic combustion chamber deposit geometries. *Intl J. Heat Fluid Flow* **69**, 83–94.

GARCÍA-MAYORAL, R., DE SEGURA, G.G. & FAIRHALL, C.T. 2019 The control of near-wall turbulence through surface texturing. *Fluid Dyn. Res.* **51** (1), 011410.

GARRATT, J.R. & HICKS, B.B. 1973 Momentum, heat and water vapour transfer to and from natural and artificial surfaces. *Q. J. R. Meteorol. Soc.* **99** (422), 680–687.

GROSSMANN, S. & LOHSE, D. 2000 Scaling in thermal convection: a unifying theory. *J. Fluid Mech.* **407**, 27–56.

GROSSMANN, S. & LOHSE, D. 2011 Multiple scaling in the ultimate regime of thermal convection. *Phys. Fluids* **23** (4), 045108.

HAMA, F.R. 1954 Boundary layer characteristics for smooth and rough surfaces. *Trans. Soc. Nav. Archit. Mar. Engrs* **62**, 333–358.

HANTSIS, Z. & PIOMELLI, U. 2020 Roughness effects on scalar transport. *Phys. Rev. Fluids* **5**, 114607.

HONG, J., KATZ, J. & SCHULTZ, M.P. 2011 Near-wall turbulence statistics and flow structures over three-dimensional roughness in a turbulent channel flow. *J. Fluid Mech.* **667**, 1–37.

JACKSON, P.S. 1981 On the displacement height in the logarithmic velocity profile. *J. Fluid Mech.* **111**, 15–25.

JAYATILLEKE, C.L.V. 1966 The influence of Prandtl number and surface roughness on the resistance of the laminar sub-layer to momentum and heat transfer. PhD thesis, Imperial College London.

JIMÉNEZ, J. 2004 Turbulent flows over rough walls. *Annu. Rev. Fluid Mech.* **36**, 173–196.

KADER, B.A. 1981 Temperature and concentration profiles in fully turbulent boundary layers. *Intl J. Heat Mass Transfer* **24** (9), 1541–1544.

KADER, B.A. & YAGLOM, A.M. 1977 Turbulent heat and mass transfer from a wall with parallel roughness ridges. *Intl J. Heat Mass Transfer* **20** (4), 345–357.

KANDA, M., KANEGA, M., KAWAI, T., MORIWAKI, R. & SUGAWARA, H. 2007 Roughness lengths for momentum and heat derived from outdoor urban scale models. *J. Appl. Meteorol. Climatol.* **46** (7), 1067–1079.

KASAGI, N., TOMITA, Y. & KURODA, A. 1992 Direct numerical simulation of passive scalar field in a turbulent channel flow. *Trans. ASME J. Heat Transfer* **114** (3), 598–606.

KATUL, G. & LIU, H. 2017 A Kolmogorov–Brutsaert structure function model for evaporation into a turbulent atmosphere. *Water Resour. Res.* **53** (5), 3635–3644.

KAWAMURA, H., OHSAKA, K., ABE, H. & YAMAMOTO, K. 1998 DNS of turbulent heat transfer in channel flow with low to medium-high Prandtl number fluid. *Intl J. Heat Fluid Flow* **19** (5), 482–491.

KAYS, W.M. & CRAWFORD, M.E. 1993 *Convective Heat and Mass Transfer*, 3rd edn. McGraw-Hill.

KOLMOGOROV, A.N. 1941 The local structure of turbulence in incompressible viscous fluid for very large Reynolds numbers. *Dokl. Akad. Nauk SSSR* **30**, 301–305.

KOZUKA, M., SEKI, Y. & KAWAMURA, H. 2009 DNS of turbulent heat transfer in a channel flow with a high spatial resolution. *Intl J. Heat Fluid Flow* **30** (3), 514–524.

KRAICHNAN, R.H. 1962 Turbulent thermal convection at arbitrary Prandtl number. *Phys. Fluids* **5** (11), 1374–1389.

LANDAU, L.D. & LIFSHITZ, E.M. 1987 *Fluid Mechanics*, 2nd edn. Pergamon.

LEONARDI, S., ORLANDI, P., DJENIDI, L. & ANTONIA, R.A. 2015 Heat transfer in a turbulent channel flow with square bars or circular rods on one wall. *J. Fluid Mech.* **776**, 512–530.

LI, Q., BOU-ZEID, E., GRIMMOND, S., ZILITINKEVICH, S. & KATUL, G. 2020 Revisiting the relation between momentum and scalar roughness lengths of urban surfaces. *Q. J. R. Meteorol. Soc.* **146** (732), 3144–3164.

LI, D., RIGDEN, A., SALVUCCI, G. & LIU, H. 2017 Reconciling the Reynolds number dependence of scalar roughness length and laminar resistance. *Geophys. Res. Lett.* **44** (7), 3193–3200.

LIN, C.C. 1959 *Turbulent Flows and Heat Transfer*. Princeton University Press.

LUCHINI, P. 1996 Reducing the turbulent skin friction. In *Computational Methods in Applied Sciences 1996, Proc. 3rd ECCOMAS CFD Conference* (ed. J.-A. Désidiri *et al.*), pp. 465–470. Wiley.

MA, G.-Z., XU, C.-X., SUNG, H.J. & HUANG, W.-X. 2020 Scaling of rough-wall turbulence by the roughness height and steepness. *J. Fluid Mech.* **900**, R7.

MACDONALD, M., CHAN, L., CHUNG, D., HUTCHINS, N. & OOI, A. 2016 Turbulent flow over transitionally rough surfaces with varying roughness densities. *J. Fluid Mech.* **804**, 130–161.

MACDONALD, M., CHUNG, D., HUTCHINS, N., CHAN, L., OOI, A. & GARCÍA-MAYORAL, R. 2017 The minimal-span channel for rough-wall turbulent flows. *J. Fluid Mech.* **816**, 5–42.

MACDONALD, M., HUTCHINS, N. & CHUNG, D. 2019 Roughness effects in turbulent forced convection. *J. Fluid Mech.* **861**, 138–162.

MARUSIC, I. & MONTY, J.P. 2019 Attached eddy model of wall turbulence. *Annu. Rev. Fluid Mech.* **51**, 49–74.

MAZZUOLI, M. & UHLMANN, M. 2017 Direct numerical simulation of open-channel flow over a fully rough wall at moderate relative submergence. *J. Fluid Mech.* **824**, 722–765.

MOSER, R.D., KIM, J. & MANSOUR, N.N. 1999 Direct numerical simulation of turbulent channel flow up to $Re_\tau = 590$. *Phys. Fluids* **11** (4), 943–945.

NIKORA, V., KOLL, K., MCLEAN, S., DITRICH, A. & ABERLE, J. 2002 Zero-plane displacement for rough-bed open-channel flows. In *River Flow 2002: Proceedings of the International Conference on Fluvial Hydraulics* (ed. D. Bousmar & Y. Zech), pp. 83–92. Balkema.

NIKORA, V., MCEWAN, I., MCLEAN, S., COLEMAN, S., POKRAJAC, D. & WALTERS, R. 2007 Double-averaging concept for rough-bed open-channel and overland flows: theoretical background. *ASCE J. Hydraul. Engng* **133** (8), 873–883.

NIKURADSE, J. 1933 Laws of flow in rough pipes. English translation published 1950. *NACA Tech. Rep.* 1292.

ORLANDI, P., SASSUN, D. & LEONARDI, S. 2016 DNS of conjugate heat transfer in presence of rough surfaces. *Intl J. Heat Mass Transfer* **100**, 250–266.

OWEN, P.R. & THOMSON, W.R. 1963 Heat transfer across rough surfaces. *J. Fluid Mech.* **15** (3), 321–334.

PEETERS, J.W.R. & SANDHAM, N.D. 2019 Turbulent heat transfer in channels with irregular roughness. *Intl J. Heat Mass Transfer* **138**, 454–467.

PEROT, J.B. 1993 An analysis of the fractional step method. *J. Comput. Phys.* **108** (1), 51–58.

PERRY, A.E. & JOUBERT, P.N. 1963 Rough-wall boundary layers in adverse pressure gradients. *J. Fluid Mech.* **17** (2), 193–211.

PIROZZOLI, S., BERNARDINI, M. & ORLANDI, P. 2016 Passive scalars in turbulent channel flow at high Reynolds number. *J. Fluid Mech.* **788**, 614–639.

POPE, S.B. 2000 *Turbulent Flows*. Cambridge University Press.

RAUPACH, M.R., ANTONIA, R.A. & RAJAGOPALAN, S. 1991 Rough-wall turbulent boundary layers. *Appl. Mech. Rev.* **44** (1), 1–25.

ROUHI, A., CHUNG, D. & HUTCHINS, N. 2019 Direct numerical simulation of open-channel flow over smooth-to-rough and rough-to-smooth step changes. *J. Fluid Mech.* **866**, 450–486.

ROUZES, M., MOULIN, F.Y., FLORENS, E. & EIFF, O. 2019 Low relative-submergence effects in a rough-bed open-channel flow. *J. Hydraul Res.* **57** (2), 139–166.

SADDOUGHI, S.G. & VEERAVALLI, S.V. 1994 Local isotropy in turbulent boundary layers at high Reynolds number. *J. Fluid Mech.* **268**, 333–372.

SCHEEL, J.D. & SCHUMACHER, J. 2014 Local boundary layer scales in turbulent Rayleigh–Bénard convection. *J. Fluid Mech.* **758**, 344–373.

SCHLICHTING, H. 1936 Experimental investigation of the problem of surface roughness. English translation published 1937. *NACA Tech. Rep.* 823.

SCHLICHTING, H. & GERSTEN, K. 2017 *Boundary-Layer Theory*, 9th edn. Springer.

SHAW, D.A. & HANRATTY, T.J. 1977 Turbulent mass transfer rates to a wall for large Schmidt numbers. *AIChE J.* **23** (1), 28–37.

SHERIFF, N. & GUMLEY, P. 1966 Heat-transfer and friction properties of surfaces with discrete roughnesses. *Intl J. Heat Mass Transfer* **9** (12), 1297–1320.

SHISHKINA, O., GROSSMANN, S. & LOHSE, D. 2016 Heat and momentum transport scalings in horizontal convection. *Geophys. Res. Lett.* **43** (3), 1219–1225.

SHISHKINA, O., HORN, S. & WAGNER, S. 2013 Falkner–Skan boundary layer approximation in Rayleigh–Bénard convection. *J. Fluid Mech.* **730**, 442–463.

SPALART, P.R., MOSER, R.D. & ROGERS, M.M. 1991 Spectral methods for the Navier–Stokes equations with one infinite and two periodic directions. *J. Comput. Phys.* **96** (2), 297–324.

SVERDRUP, H.U. 1951 Evaporation from the oceans. In *Compendium of Meteorology* (ed. T.F. Malone), pp. 1071–1081. Springer.

TENNEKES, H. & LUMLEY, J.L. 1972 *A First Course in Turbulence*. MIT Press.

THAKKAR, M., BUSSE, A. & SANDHAM, N.D. 2018 Direct numerical simulation of turbulent channel flow over a surrogate for Nikuradse-type roughness. *J. Fluid Mech.* **837**, R1.

TOWNSEND, A.A. 1976 *Turbulent Shear Flow*. Cambridge University Press.

VERSTAPPEN, R.W.C.P. & VELDMAN, A.E.P. 2003 Symmetry-preserving discretization of turbulent flow. *J. Comput. Phys.* **187** (1), 343–368.

WARHAFT, Z. 2000 Passive scalars in turbulent flows. *Annu. Rev. Fluid Mech.* **32** (1), 203–240.

WEBB, R.L., ECKERT, E.R.G. & GOLDSTEIN, R.J. 1971 Heat transfer and friction in tubes with repeated-rib roughness. *Intl J. Heat Mass Transfer* **14** (4), 601–617.

WEI, T. 2018 Multiscaling analysis of the mean thermal energy balance equation in fully developed turbulent channel flow. *Phys. Rev. Fluids* **3** (9), 094608.

WYNGAARD, J.C. 2010 *Turbulence in the Atmosphere*. Cambridge University Press.

YAGLOM, A.M. 1979 Similarity laws for constant-pressure and pressure-gradient turbulent wall flows. *Annu. Rev. Fluid Mech.* **11** (1), 505–540.

YAGLOM, A.M. & KADER, B.A. 1974 Heat and mass transfer between a rough wall and turbulent fluid flow at high Reynolds and Péclet numbers. *J. Fluid Mech.* **62** (3), 601–623.

YANO, T. & KASAGI, N. 1999 Direct numerical simulation of turbulent heat transport at high Prandtl numbers. *JSME Int. J.* B **42** (2), 284–292.

ZHOU, Q., STEVENS, R.J.A.M., SUGIYAMA, K., GROSSMANN, S., LOHSE, D. & XIA, K.-Q. 2010 Prandtl–Blasius temperature and velocity boundary-layer profiles in turbulent Rayleigh–Bénard convection. *J. Fluid Mech.* **664**, 297–312.